The Dissertation Committee for Changhyun Ryu
certifies that this is the approved version of the following dissertation:

Photoassociation Experiments on Ultracold and Quantum Gases in Optical Lattices

Committee:

Daniel J. Heinzen, Supervisor

Manfred Fink

Greg O. Sitz

Qian Niu

Robert E. Wyatt

Photoassociation Experiments on Ultracold and Quantum Gases in Optical Lattices

by

Changhyun Ryu, B.S., M.S.

DISSERTATION

Presented to the Faculty of the Graduate School of
The University of Texas at Austin
in Partial Fulfillment
of the Requirements
for the Degree of

DOCTOR OF PHILOSOPHY

THE UNIVERSITY OF TEXAS AT AUSTIN
August 2004

To my wife Hyunkyung and my parents

Acknowledgments

First of all, I'd like to thank Prof. Heinzen for his guidance and support for the research done in this thesis. His enthusiasm and insight in physics made this project possible.

Most of work done in this thesis would not be possible without the help from present and past group members. Dr. Riley Freeland and Dr. Roahn Wynar taught me everything I need to know to do the experiment and their patience and willingness to help me in understanding how to work in the lab was essential in my development as a physicist. Also I learned a lot from Dr. Daniel Comparat and Dr. Gang Xu in various aspects of experimental and theoretical work in the lab.

Wooshik Shim and Nathan Harrison helped me a lot in a difficult task of putting things together for the new BEC experiment. Especially the beautifully built magnetic trap which is essential to the BEC experiment could not be possible without them. Dr. Xu Du, Emek Esilida, and Shoupu Wan (current BEC group members) were really helpful in finishing this project and their commitment and ingenuity which advanced this project will make it possible to achieve many great things in the future.

It would probably not be possible to finish this work without the support from my wife Hyunkyung. Her understanding and appreciation of my

work in physics was essential in any success I have in this thesis. I also would like to thank my parents for giving me support and trust which helped me overcome the difficult days of my graduate school.

Photoassociation Experiments on Ultracold and Quantum Gases in Optical Lattices

Publication No. ____________________

Changhyun Ryu, Ph.D.
The University of Texas at Austin, 2004

Supervisor: Daniel J. Heinzen

This thesis describes the results of several experiments that studied the photoassociation of an ultracold atomic Rb gas. In the first experiment, we produced ultracold diatomic molecules from an atomic gas via single-color photoassociation. The molecules were detected with resonance-enhanced multiphoton ionization. Trapping of these molecules in a quadrupole magnetic trap, with lifetimes up to 20 seconds, was also demonstrated. In addition, the rate constant for inelastic collisions between the trapped molecules and atoms was determined from measurements of the atomic density dependence of the decay rate of the trapped molecules.

In another experiment, stimulated Raman photoassociation of Rb atoms in a Mott insulator state was studied. A Bose-Einstein condensate (BEC) of 87^{Rb} atoms was loaded into a three-dimensional optical lattice formed by the interference pattern of three orthogonal standing wave laser fields. This system constitutes a very good realization of the Bose-Hubbard model, which predicts a quantum phase transition between a superfluid state and a Mott insulator state at a particular lattice height. A time-of-flight imaging method was used to study the state of the atomic gas, and the quantum phase transition was observed at the predicted lattice height. The signature of the phase transition was the disappearance and reappearance of peaks in the image that arose from the interference of atoms originating from different lattice sites. Two coherent laser fields were applied to the gas in its Mott insulating state, and tuned close to a Raman photoassociation resonance, and this resulted in an observable loss of atoms due to the formation of molecules. This transition exhibited a double-peaked spectrum, with one of the peaks arising from photoassociation of atoms in sites containing only two atoms, and the other from sites containing three atoms. Also, the loss of atoms vs. the duration of the Raman photoassociation period was studied, with the lasers tuned to the peak corresponding to two atoms per site. It was found that a central core of the gas, containing about 40 percent of the atoms, exhibited a coherent oscillation between an atomic and molecular quantum gas.

Table of Contents

List of Tables

List of Figures

Chapter 1

Introduction

Superconductivity and superfluidity are two of the most amazing discoveries in 20th century physics [1]. Both effects show the macroscopic quantum effect and come from the very similar physics of BEC(Bose-Einstein Condensate). Superfluidity of ^{4}He comes from the Bose-Einstein Condensate of ^{4}He atoms and superconductivity can be thought of as a BEC of cooper pairs. But the direct and clear observation of a BEC in condensed matter systems was very difficult due to strong interactions. Only after many decades of hard work and creative innovations in laser cooling and trapping of a dilute atomic gas [2], a BEC of a dilute gas was observed in 1995 [3] [4]. A dilute gas BEC made it possible to study a BEC in an ideal condition and also coherent atoms from a BEC are perfect source for coherent matter wave experiments. There has been an explosive growth in BEC physics and it is expected to grow more in the future [5]. Another fascinating new development is the realization of quantum degenerate fermionic atoms and research toward the realization of BCS cooper pairs with ultracold atoms [6] [7] [56]. This research actually has the possibility of studying condensed matter systems with atomic physics system and the list of possible experiments are growing everyday.

1.1 Ultracold molecules

After the impressive progress in atomic physics with ultracold atoms, it is natural to ask what can be achieved with ultracold molecules. There are many interesting proposals for ultracold molecules. At a ulracold temperature, chemical reactions between atoms and molecules will have different characteristics and it will be interesting to study these effects [9]. There are also a couple of interesting proposals using ultracold polar molecules. It was suggested that by using dipole interaction between ulracold polar molecules trapped in an optical lattice, a scalable quantum computer can be built [30]. Also because of a very big enhancement of the electron EDM (electric dipole moment), ultracold polar molecules are very interesting choice for the electron EDM search [11].

Although a BEC of bosonic atoms and a quantum degenerate gas with fermionic atoms were achieved and studied extensively, it will be interesting to study the same physics with molecules. Because of the complicated inner structure of molecules, there is a possibility of studying quantum degenerate gas of molecules with anisotropic interactions and this system predicts many interesting phenomena [12]. Also studying conversion of atoms into molecules itself is very interesting because this corresponds to the second harmonic generation in a matter wave and opens the possibility of coherent coupling between atoms and molecules which is called "Superchemistry" [13].

However, molecules lack closed transitions which are essential for laser cooling. There are several different ways of making ultracold molecules and trapping them. One way of producing molecules is using another cooling technique which can be applied to diverse atomic and molecular species. Buffer gas cooling is the first method used to cool hot molecules and trap them in a magnetic trap [14]. Helium buffer gas at very cold temperate is used to cool hot molecules with elastic collisions. J. Doyle group at Harvard pioneered in this technique to produce cold molecules. The big advantage of this method is that this method can be applied to any atom or molecule which has a magnetic moment. With this method, the number of molecules trapped is about 10^8 and the temperature is around 300 mK. Another method to cool molecules is a stark decelerator which uses inhomogeneous electric field to reduce the kinetic energy of polar molecules [15]. With the clever switching on and off of the electric field, it is possible to have molecules always climb up the potential barrier. With this method, NH_3 molecules were cooled and trapped in an electric field. The temperature achieved was about 350 mK. The advantage of these two methods is the possibility of the general application of these techniques. Also molecules are produced and cooled in a ro-vibrational ground state. But as we can see from the temperature achieved so far, there is a long way to go to catch up the temperature of ultracold atomic gas which can be as low as a few nK. Also the possibility of an evaporative cooling needs to be shown.

The second method of creating ultracold molecules uses the well established technique of creating ultracold atoms as a starting point and converts these atoms into molecules. There are two ways of converting atoms into molecules. One is using Feschbach resonance [16] [18] [17]. Feschbach resonance is the resonance betwee a bound molecular state and two free atomic state achieved by the variation of the energy difference between these two states which have different Zeeman energy shifts controlled by an external magnetic field. By sweeping this magnetic field atoms can be converted into molecules adiabatically. The second way of converting atoms into molecules is by photoassociation [19] [20]. During photoassociation process, two colliding atoms will absorb a single photon from a photoassociation laser beam whose energy is equal to the excited molecular state energy and these two atoms will be converted into an excited state molecule. These excited state molecules can decay into singlet ground state or triplet ground state molecules depending on the symmetry of an excited molecular state. Or Raman photassociation can be used to convert these excited molecules into the specific ro-vibrational state molecules. R. Knize first trapped Cs_2 molecules produced from a MOT [21] and there are many experiments to detect molecules produced via a photoassociation [22] [23] [24] [25]. Also magnetic trapping of Cs_2 produced by photoassociation was also reported [26].

The common problem for both methods is the fact that the created molecules are mostly in highly excited vibrational states. Because these molecules in high lying vibrational levels can collide with other atoms and molecules and decay into deeply bound vibrational states, inelastic collisions limit the efficiency and stability of molecules produced. But if the produced molecules can be transferred to a ro-vibrational ground state, we will have a very stable ultracold molecular gas.

1.2 Ultracold atoms in an optical lattice

The advantage of the ultracold atomic system over the liquid helium system to study BEC is the weak interaction between atoms compared to the strong interaction between helium atoms. Because of this weak interaction , a pure BEC can be observed and coherent atoms can be produced from a BEC. There have been many exciting results from the study of an weakly interacting atomic system. Another interesting possibility of the atomic system is the ability of controlling the strength of the interaction between atoms. A Feshbach resonance mentioned earlier can be used to change the interaction strength between atoms [27]. We can increase effective interaction between atoms by increasing the confinement of atoms and an optical lattice is an ideal system to increase the confinement. Many condensed matter systems are strongly interacting systems and it will be very interesting to study strongly interacting and correlated systems with ultracold atoms. The system of ultracold atoms in an optical lattice turns out to be a very promising system to study a strongly interacting many body system . There are many advantages of using atomic system to study a strongly interacting many body system. We can eliminate the impurities in an atom system very easily and the parameters of an interacting many body system can be adjusted easily in an atomic system.

Ultracold atoms in an optical lattice can be described with a Bose-

Hubbard model which predicts a quantum phase transition from a superfluid to a Mott insulator [28] . Recently, a quantum phase transition from a superfluid to a Mott insulator was realized with ultracold atoms in an optical lattice [29]. There are many interesting theoretical proposals to study this quantum phase transition with several different configurations of ultracold atoms in an optical lattice [30] [31]. Also a dilute gas Mott insulator with one atom per lattice site is a perfect starting point for the quantum information processing with neutral atoms [32]. There is also a growing interest in a strongly interacting 1-D Bose gas which can be realized with ultracold atoms in a 2-D lattice. A strongly interacting one dimensional bosonic gas is predicted to behave like non interacting fermionic gas [33] [34]. Experimental realization of this system will be very interesting.

Another interesting possibility is to study ultracold fermionic atoms in an optical lattice [35] [36]. There is a theoretical study of this system in 2-D and 3-D optical lattices and it was shown that ultracold fermionic atoms in a 2-D optical lattice exhibit high-Tc superconductivity [35]. Unlike other examples, the exact nature of high-Tc superconductivity is unknown at this time and experiments with ultracold fermionic atoms in a 2-D optical lattice will make it possible to understand the nature of high-Tc superconductivity with an atomic system. This shows that studying ultracold aotms in optical lattices can be a powerful tool in understanding interesting phenomena and new physics in strongly interacting and correlated many body systems.

1.3 Main results of this work

This thesis consists of three experiments. The first experiment presented in this thesis is ultracold molecule formation and trapping experiment. We created ultracold ^{87}Rb$_2$ molecules in a triplet ground state via a single photon photoassociation. Due to the very favorable Franck-Condon factor, we can create ultracold molecules efficiently. These created molecules were detected with a REMPI (Resonance Enhanced Multi-Photon Ionizatin) method. The temperature of molecules in a trap was measured to be 198μK and the number of trapped molecule was 4×10^3. The atom-molecule inelastic collision rate was measured and $K_{am} = 3.45(\pm 0.93) \times 10^{-11}$ s/cm^3. Without atoms, we could trap molecules with a 20 s lifetime in a magnetic trap. However the lifetime of molecules inside a BEC of atoms will be shorter than 1 ms because of a high density of atoms in a BEC which is typically 10^{14} cm^{-3}. This measurement showed the difficulty in making ultracold molecules from a BEC due to the inelastic collisions. New BEC set up was made to improve the old BEC set up and to make it possible to set up a 3-D optical lattice. New BEC chamber and new cloverleaf type magnetic trap was designed and built for the new experiment. With this new set up, a pure BEC with 2 million ^{87}Rb atoms could be produced.

A 3-D optical lattice was set up to study a quantum phase transition from a superfluid to a Mott insulator with ultracold atoms in an optical lattice. Ultracold atoms in an optical lattice can be described with a Bose-Hubbard hamiltonian which predicts a quantum phase transition from a superfluid to a

Mott insulator. A quantum phase transition was observed with a TOF (Time Of Flight) absorption imaging. In a superfluid state, matter wave interference peaks were observed and there were no interference peaks in a Mott insulator state. A careful study of widths of central peaks change shows an increase when the system enters a Mott insulator state. Also we observed the depletion of a BEC as we increase the an optical lattice depth.

Raman photoassociation was applied to a Mott insulator of an atomic gas to produce ultracold molecules in an optical lattice. Because of a very small tunnelling rate between adjacent sites in a Mott insulator state, there were no inelastic collisions between atoms and produced molecules. Raman resonance frequency shift between two atoms per site Mott insulator and three atoms per site Mott insulator was observed. By locking the Raman frequency to two atoms per site Mott insulator Raman resonance frequency, we observed coherent Rabi oscillations between atoms and molecules in an optical lattice. This is the clear signature of coherent creation of molecules from atoms and this will be the first step toward the creation of a quantum molecular gas in an optical lattice.

Chapter 2

Ultracold molecule production and trapping

There have been impressive rapid developments in atomic physics since the invention of laser cooling and trapping. It will be very interesting to see what can be achieved with the creation of ultracold molecules.

As discussed in previous chapter, there are a few methods of producing ultracold molecules. In this chapter, we will discuss the ultracold molecule formation from a single color photoassociation and magnetic trapping of ultracold molecules. Also we will show the measurement of an atom-molecule inelastic collision rate and discuss the implication of this measurement in the future experiments.

2.1 Experimental set up

This experiment was done with an experimental set up that was built by former students Dian-Juin Han [37] and Roahn Wynar [38]. A good description of this apparatus can be found in their thesis. ^{87}Rb atoms were slowed by a Zeeman atomic beam slower and loaded into a MOT (Magneto-Optical Trap). Since a photoassociation rate is proportional to the density of atoms, it's important to increase the density to have efficient molecule production. In a MOT, main limitation of density of atoms is the effect of radiation trapping when atoms reabsorb photons emitted by other atoms. To solve this problem, so called a dark MOT was invented [39]. In a dark MOT atoms remain in a dark hyperfine ground state which is F=1 state for ^{87}Rb atoms and do not absorb photons from MOT beams because the repumper beam that pumps atoms into F=1 state has a hollow center. But outside of this hollow center atoms will absorb photons from MOT beams and be trapped. This is a very successful technique to increase the density of atoms in a MOT and we adopted this in our experiment to increase the photoassociation rate which is proportional to the density of atoms. Produced molecules were trapped in a quadrupole magnetic trap which was generated by two circular coils inside the chamber which generate the usual radial gradient value of 60 G/cm.

We used a Ti-Sapphire laser (Coherent model 899-01) to produce a photoassociation laser beam. This laser was converted to a single frequency laser and stabilized by locking into an optical cavity whose length was stabilized by a MOT laser. Using this locking set up, we could tune the laser frequency to any desired value and hold it fixed within 1 MHz over several hours. The detail of this locking system is available in Roahn Wynar's thesis [38]. We used an optical fiber to transfer the beam from a laser optical table to the experiment optical table. At the location of the atomic cloud, the waist of beam was 1.1 mm and we usually used 150 mW laser beam power for the photoassociation experiment.

Produced molecules were detected with the method of REMPI (Resonant Enhanced Multi Photon Ionization). Molecules can be excited into an ionized state with an absorption of several photons and if one or more photon energy matched the energy difference between different intermediate states, the transition will be enhanced. We used photons from pulsed dye laser pumped by pulsed Nd:YAG laser to do REMPI measurement.

The Nd:YAG laser we used is Lab 170 from Coherent with 30Hz repetition rate. The maximum pulse energy was 210 mJ at 355nm and 330 mJ at 532 nm. Dye laser was Sirah Cobra Stretch (model CSTR-LG-18). We used a dye laser beam which had a waist of 1.24 mm at the location of cloud and typical energy per pulse was 10-15 mJ. To detect ions produced, we used channeltron ion detector which we installed inside the chamber. The detail of this set up is available in Riley Freeland's thesis [40].

2.2 Formation and trapping of ultracold molecules

Photoassociation is a process of conversion from two free atoms to an excited sate molecule via an absorption of a single photon. These excited state molecules have usually very short lifetimes, typically about 12 ns. Molecules can decay into continuum states of two free atoms, into singlet molecular states, or into triplet molecular states. We are trying to trap molecules produced in a magnetic trap which means that it's necessary for us to create large number of triplet state molecules which will have a magnetic moment. Transition strength between different states are determined by dipole matrix element and Franck-Condon factor which is determined by vibrational wavefunctions

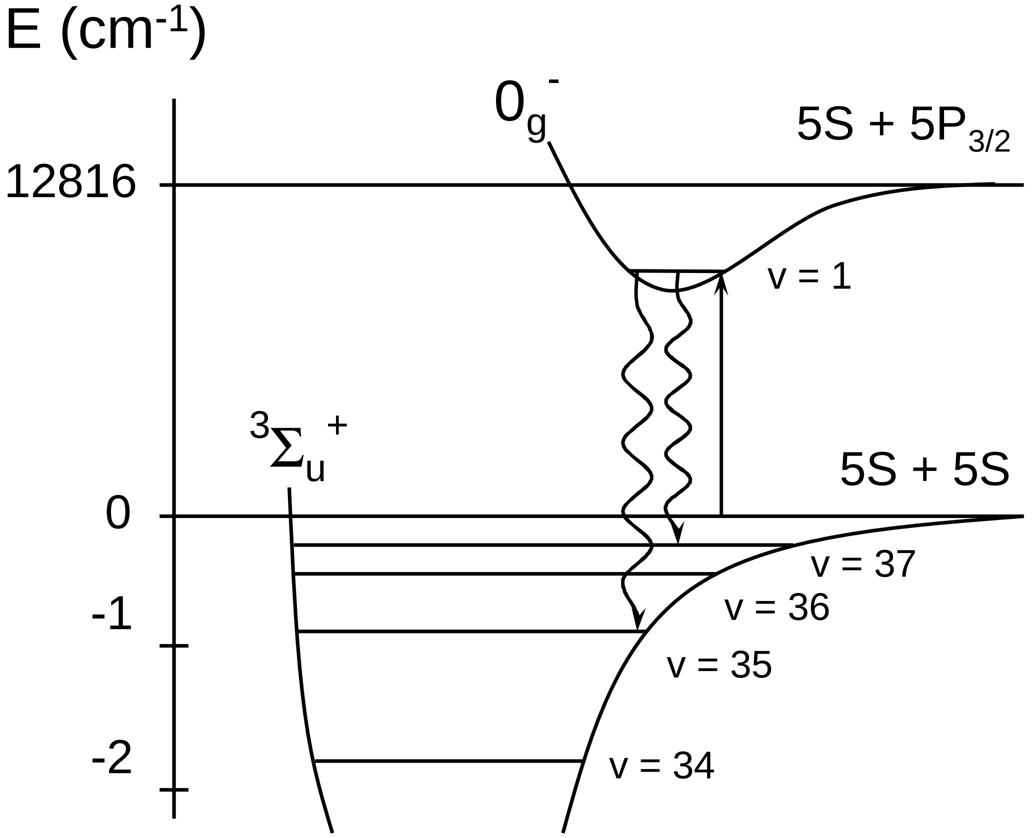

Figure 2.1: One color photoassociation binds two colliding atoms with a photon to form an excited state molecule. When $\omega = \omega_0 - \Delta - E$ the process is resonant. The excited state decays at a rate γ producing either hot atoms or bound ground state molecules.

Table 2.1: Theoretical calculation of binding energies, outer turning point , and Frack-Condon factor to 0_g^-(v=1) excited state of ground state vibrational levels

v	Binding Energy (GHz)	Outer Turning Point(a_0)	Franck-Condon Factor (to 0_g^-(v=1))
40	0.024	104.28	0.003
39	0.63	60.22	0.032
38	2.93	46.83	0.135
37	8.05	39.72	0.321
36	17.15	35.16	0.077
35	31.35	31.92	0.118
34	51.77	29.48	0.042
33	79.48	27.56	0.002

of each state. Fig. 2.1 shows schematic of the formation of ultracold molecules via photoassociation.

It is important to select an excited state which has a good overall transition probability into triplet ground state molecules. We calculated some of these Franck-Condon factors and Tab. 2.1 shows the result for the $0_g^-(v = 1, \mathrm{P}_{3/2})$ state we used in this experiment. This potential is sometimes called "pure long range potential", because the equilibrium position is located further out than the usual molecular potentials. The high lying vibrational level states in triplet potential have similar turning points as the excited state we chose. Because of this, Franck-Condon factors are very favorable in producing triplet ground state molecules in high lying vibrational levels. Especially $v = 37$ which has a binding energy of 8 GHz receives more than 30 % of a total decay.

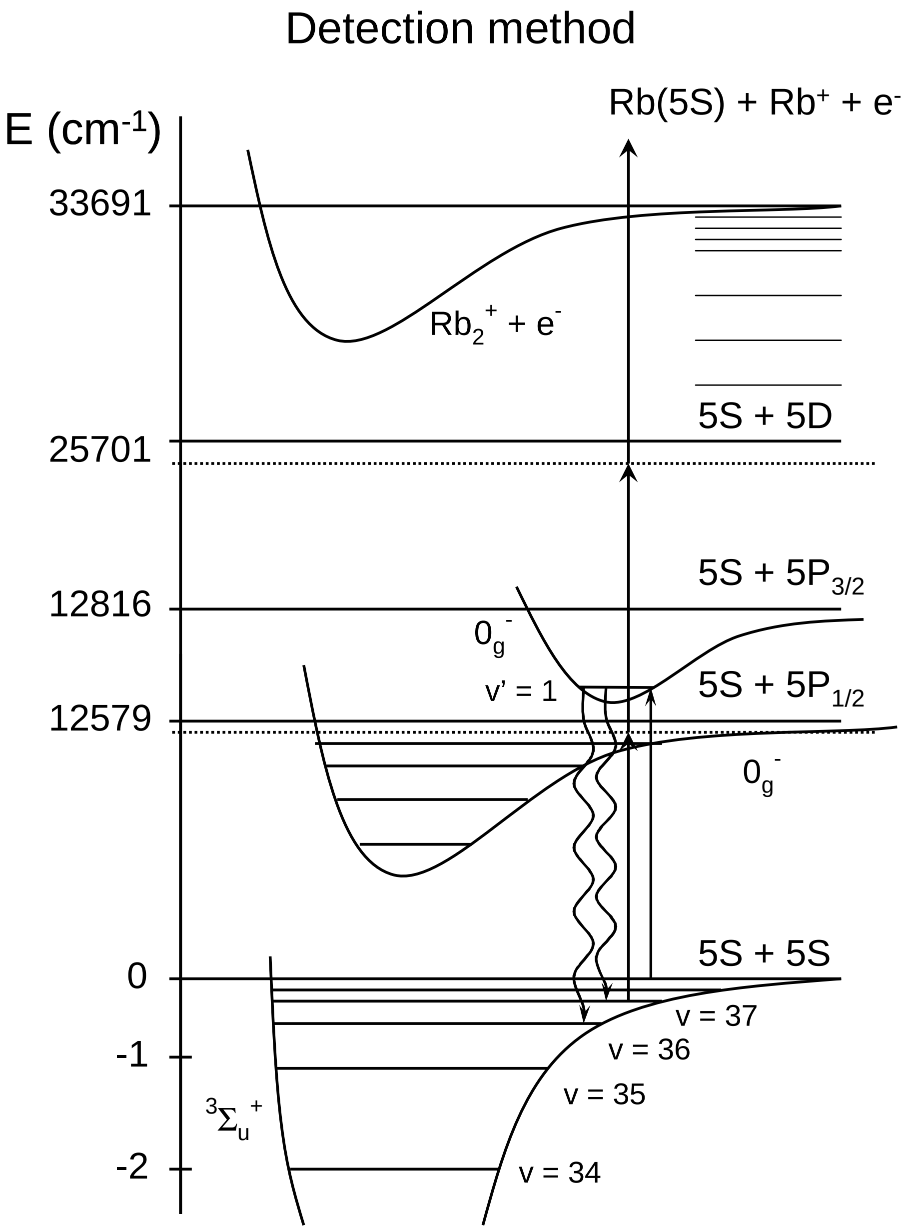

Figure 2.2: Resonant Enhanced Multi Photon Ionization (REMPI) process of Rb molecules

2.2.1 Multi-photon ionization detection of molecules

In previous experiments, molecule formation was detected from the decrease of the number of atoms. But this method can not be used if we want to measure the decay rate of trapped molecules. We decided to implement the direct detection of molecules with a multiphoton ionization method. In a previous work by Riley Freeland, a pulsed dye laser with wavelength around 600 nm was used to detect molecules. But we realized that the ionization efficiency of 600 nm dye laser is not very good for high lying vibrational levels. We tried to have a two color ionization method with 355nm pulsed laser beam from 3rd harmonic of Nd:YAG laser pulse and dye laser pulse with wavelength range of 780nm-810nm. We tried various configurations to find out the best combination to increase the molecule signal. The biggest problem we had with this two color ionization scheme was the background signal from the ionizations of atoms. The excited state atoms can be ionized very easily with 355nm Nd:YAG laser pulses. Dye laser pulse had a ASE (Amplified Spontaneous Emission) spectrum which included Rb D1 and Rb D2 resonance frequencies. This meant that atoms got excited by a dye laser pulse and got ionized by a 355nm Nd:YAG laser pulse. Although this process was not very efficient, the ions from this process was much bigger than the molecule signal because the number of atoms was much larger than the number of molecules. It turned out that the best way to get a big signal without too much background signal is just using a pulsed dye laser only for the ionization. Molecules could be ionized with three photons from a dye laser pulse and this three photon ionization process could be enhanced by resonance. Fig. 2.2 shows the REMPI (Resonance Enhanced Multi Photon Ionization) method we used.

To find out the best dye laser wavelength to optimize the molecule signal, molecules were produced and detected in a dark MOT. There was a few ms delay between the photoassociation pulse and the dye laser pulse to detect only triplet ground state molecules. Although the molecules produced were not trapped , this was a very convenient way to optimize the photoassociation process and the detection scheme. Especially to see the signal change as a function of the dye laser wavelength, we fixed the photoassociation laser frequency, power, and pulse duration. The signal change as a function of the dye laser wavelength is plotted in Fig. 2.3.

The complicated structure in this spectrum came from the combined effect of triplet ground state population distribution in different vibrational levels and excited state structure. We decided to use 805.5 nm for the dye laser wavelength which is corresponding to the biggest peak to maximize the signal from molecules. We did the fine scale scan around this peak and Fig. 2.4 shows the width of this peak to be about 7 GHz. The narrow width of this peak suggested that only one or two triplet ground state vibrational levels were involved in this ionization process.

2.2.2 Magnetic trapping of ultracold molecules

Triplet ground state molecules can have magnetic moments which are necessary for the magnetic trapping that uses the inhomogeneous magnetic

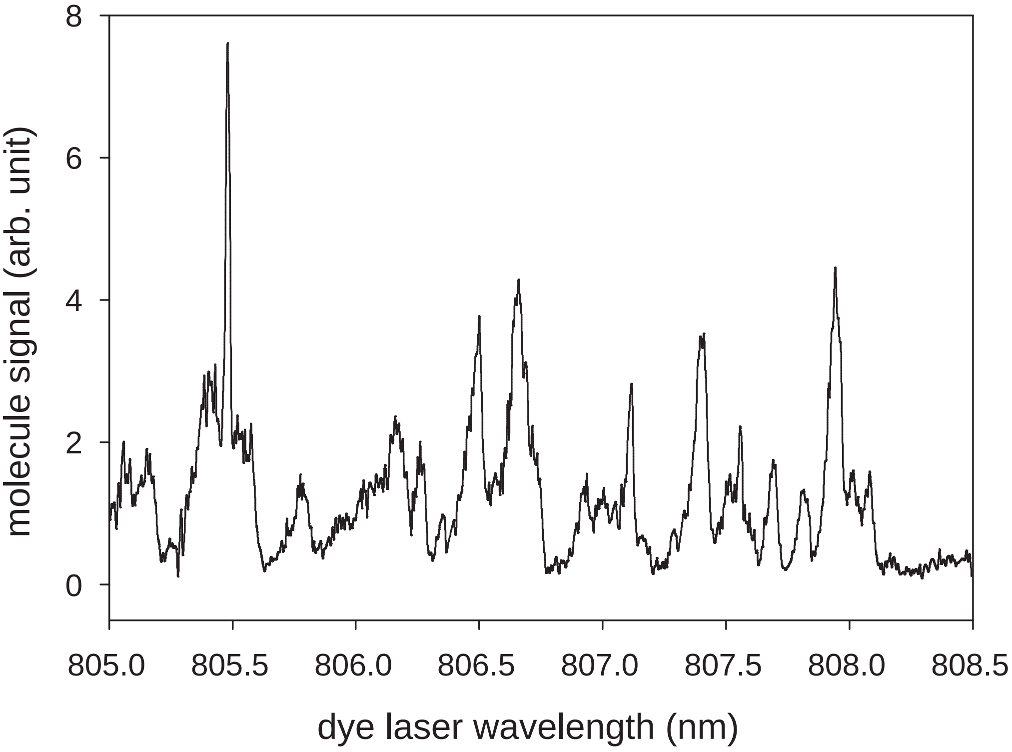

Figure 2.3: Ionization spectrum

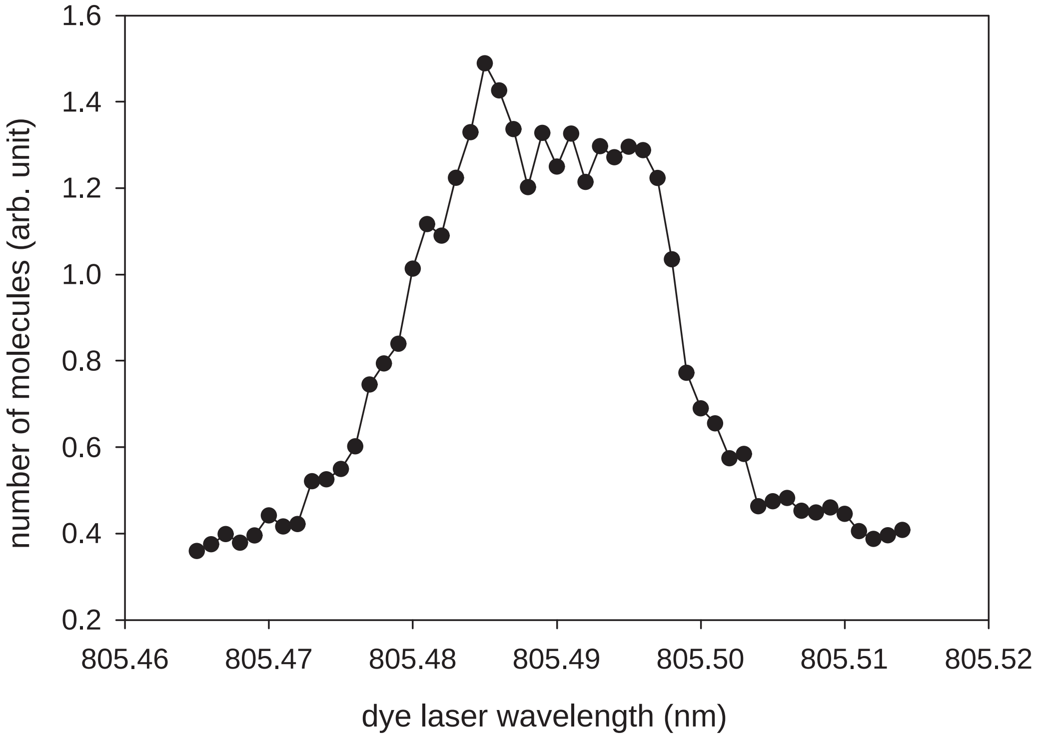

Figure 2.4: Fine resolution ionization scan

field to trap molecules or atoms with magnetic moments. Magnetic trapping of cold molecules was demonstrated earlier by Doyle group [14]. But the lifetime of molecules in this trap was very short and no systematic study of the limitation of the lifetime was done.

In the previous chapter, molecules were produced and detected in a dark MOT. These produced molecules can be trapped in a magnetic trap if we turned on the magnetic trap suddenly after the production of molecules. Or atoms in a dark MOT can be transferred to a magnetic trap and molecules were produced and trapped in the magnetic trap. Both methods gave us the trapping of ultracold molecules and the only difference we found was that two or three times more molecules were produced and trapped with the method of creating ultracold molecules in the dark MOT. This may be due to the temporarily high density of atoms in the dark MOT compared to the steady state density of atoms in the magnetic trap. The higher signal we saw in the molecule formation from tbe dark MOT cloud began to get smaller if we increased the dark MOT duration. In steady state dark MOT, the signal was much smaller than the case of temporal dark MOT for 150 - 300 ms. We observed similar effect of density change as a function of dark MOT duration in our new BEC experiment and this will be discussed in Ch.3.

To make sure that we produced molecules which are trapped in the magnetic trap, we tried to find out the spatial distribution of molecules trapped in a magnetic trap after 75 ms trapping. 75ms is long enough time for most of the molecules which were not trapped to leave the trap due to free falling and thermal expansion. We focused the size of the dye laser beam down to $\omega_0 = 0.43$mm and scaned the dye laser beam across the molecule cloud and measured the ion signal as a function of the location of the beam inside the cloud. Fig. 2.5 shows a typical example of this measurement. This data clearly shows that we have trapped molecules in a magnetic trap.

Trapping potential for molecules in a quadrupole magnetic trap including a gravity can be written as

$$U(r,z) = -\mu_m \mathrm{B}'_r \sqrt{\rho^2 + 4z^2} + 2mgz \tag{2.1}$$

The fact that we can trap molecules suggest that molecules have magnetic moments and we tried to estimate the magnitude of this magnetic moment by measuring the number of molecules dependence on the magnetic field gradient. Because of gravity, there is a minimum magnetic field gradient value along z direction to have a trap for atoms and molecules. The minimum gradient along vertical direction to support a trap is $\mathrm{B}'_z = \frac{mg}{\mu}$. Atoms are in $F = 1$ and $m_F = -1$ state. This state has a magnetic moment of one half Bohr magneton. We can calculate the minimum radial gradient value which supports the trap for atoms which is 15.37G/cm. Data in Fig. 2.6 supports this calculation. Atoms in $F = 1$ and $m_F = -1$ state can yield molecules that can have total spin from $F = 4$ to $F = 0$ and can have various Zeeman states. The exact branching ratio will be determined by various transition probability calculation but it is clear that there are some molecular state which can be

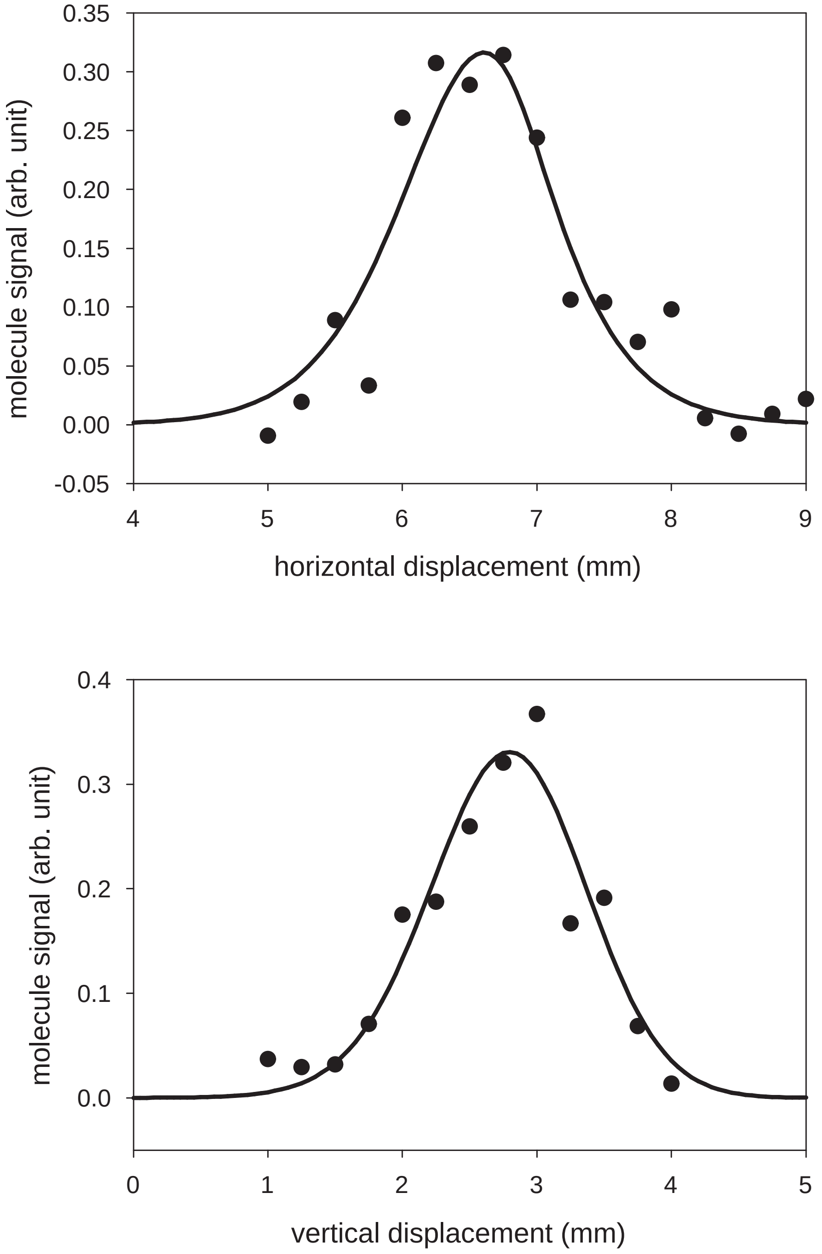

Figure 2.5: Horizontal and vertical distributions of trapped molecules and fitting based on thermal equilibrium distributions

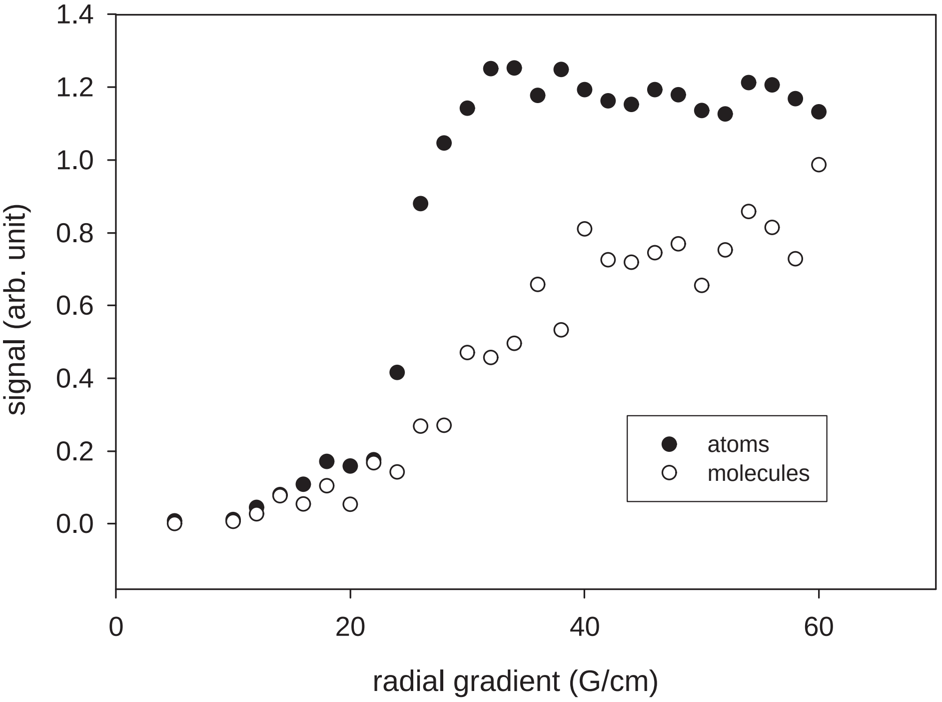

Figure 2.6: The change of the number of trapped atoms and molecules as a function of radial gradient

trapped. Fig. 2.6 shows that there is no trap for molecules below 20 G/cm and this data is consistent with the assumption that magnetic moment of molecules is one Bohr magneton which is twice the atomic magnetic moment.

If we assume that molecules are in thermal equilibrium in the trap and in a single magnetic state, we can get the information of the temperature of molecules by fitting measured spatial distribution with theoretical model of a density distribution in a magnetic trap.

$$n_a(\rho, z) = n_{a,0}(t)e^{-\frac{\mu_a \mathrm{B}'_r}{k_B T}\sqrt{\rho^2+4z^2}+mgz} \tag{2.2}$$

$$n_m(\rho, z) = n_{m,0}(t)e^{-\frac{\mu_m \mathrm{B}'_r}{k_B T}\sqrt{\rho^2+4z^2}+2mgz} \tag{2.3}$$

By assuming a gaussian beam for the dye laser with $\omega_0 = 0.43$mm and a molecular magnetic moment of one Bohr magneton, the spatial distribution was fitted with a theoretical function and found that temperature is about $198(\pm 46)\mu K$ which is a little bit higher than atomic temperature which we measured to be $117(\pm 12)\mu K$. Fig. 2.5 shows this data and fitting. This data shows that molecules were trapped at a ultracold temperature. No direct measurement of thermalization between atoms and molecules was done but considering the thermalization rate of atoms at the same density, it is very likely that molecules are in thermal equilibrium with atoms.

If we assume that in fact molecules and atoms have a same temperature, the temperature difference from the fitting might come from the assumption of gaussian beam shape of the pulsed dye laser which has a very complicated beam shape and the effect of saturation also needs to be considered. Also it is possible that magnetic moment of molecules may be smaller than we thought.

Next question for us was how long molecules will live in a trap. Molecular lifetime was measured by measuring a molecule signal as a function of waiting time. Fig. 2.7 shows a typical decay curve of trapped molecules with atoms in the magnetic trap. The lifetime of trapped molecules was much shorter than atomic lifetime which is 50 s at the same chamber pressure. To check the effect of atom-molecule inelastic collisions, we removed atoms after

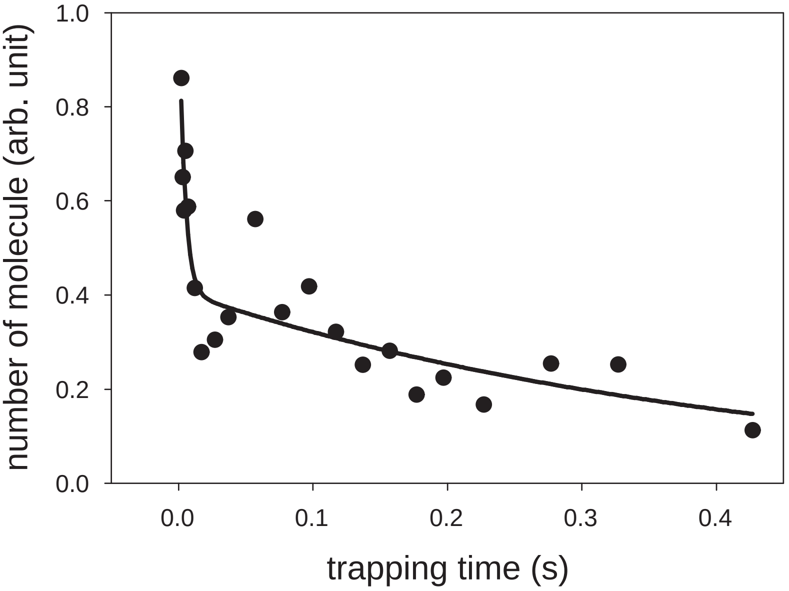

Figure 2.7: Decay of trapped molecules with atoms. The solid line is a double exponential decay fitting curve. The fast decay life time is 4.3 ms and the slow decay life time is 419 ms. The fast decay component is from molecules which are not trapped and the slow decay component is from molecules which are trapped in the magnetic trap.

molecules were created with a resonant laser pulse. Without atoms in the trap, the lifetime of the molecules increased up to 20 s. This is the clear evidence of the existence of the inelastic collisions between atoms and molecules which will be discussed in the next chapter.

Fig. 2.8 shows the decay curve of molecules trapped in a magnetic trap without atoms at two different chamber pressures. We can clearly see that there was a difference in decay rate as a function of pressure of the chamber. This suggests that most of molecular decay process came from the background gas collisions with molecules. The difference between atomic lifetime and molecular lifetime may come from the difference in the collisional cross-section.

2.3 Atom-molecule inelastic collisions

2.3.1 Estimation of the number of molecules

To determine the atom-molecule inelastic collision rate, we need to know the number and density of atoms and molecules. We can determine the number and density of atoms using a standard TOF absorption imaging method. And if we know the formation rate and decay rate of molecules, we can determine the steady state number of molecules we produced.

$$\frac{dn_m}{dt} = \frac{K_{PA}}{2} n_a^2 f_m f_v - \Gamma_m n_m \tag{2.4}$$

K_{PA} is the photoassoication loss rate and one photoassociation event will remove two atoms from an atomic cloud. f_m is the fraction of molecules

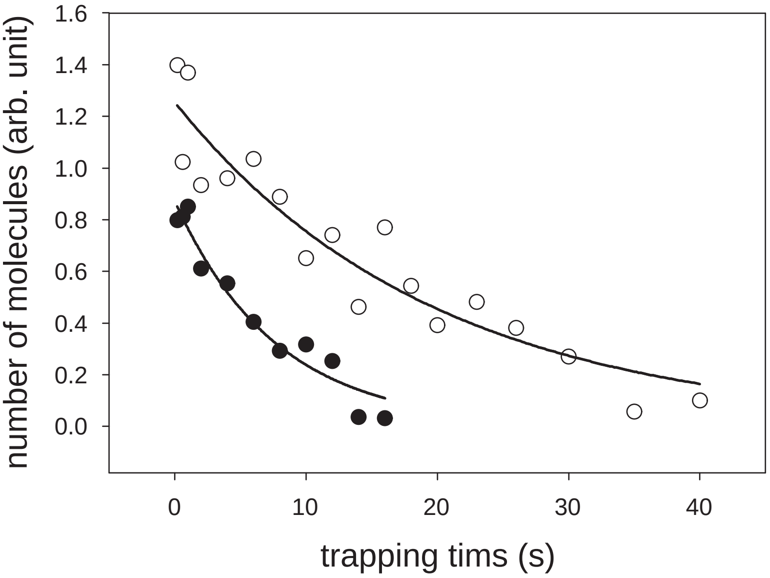

Figure 2.8: Decay of trapped molecules without atoms at two different pressures of the chamber. The faster decay curve was taken at the pressure of 1.1×10^{-10} torr and the slower decay curve was taken at the pressure of 3.6×10^{-11} torr. The exponential decay rates were 0.0412 s^{-1} and 0.0188 s^{-1} respectively.

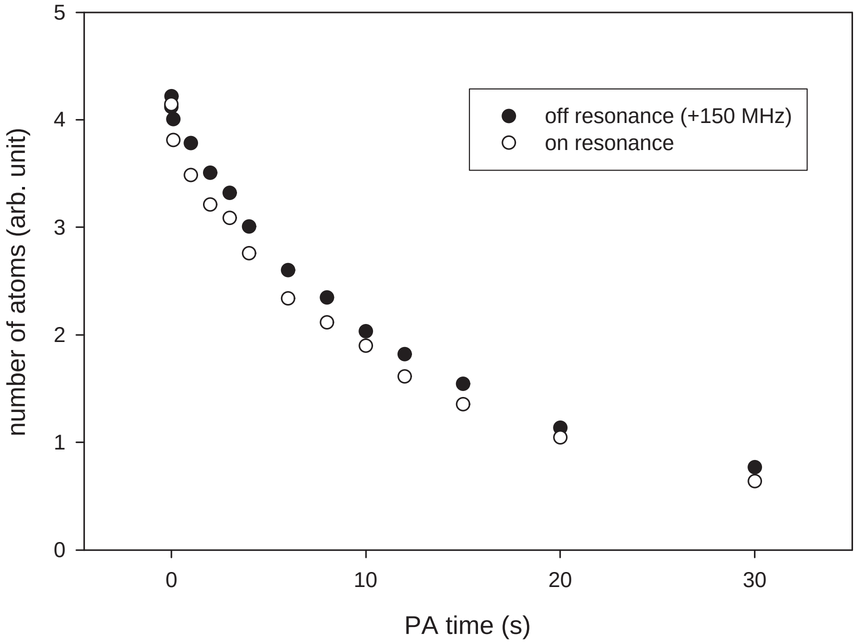

Figure 2.9: Decay of trapped atoms with photoassociation laser on with two different detunings from the excited state

which will be trapped and f_v is the fraction of molecules decayed into the specific vibration level we are detecting. Γ_m is the decay rate of molecules produced during the photoassociation pulse. We found that the decay rate coming from background gas collisions and atom-molecule collisions is much smaller than the decay rate of molecules from scattering of photoassoication laser. We can do the spatial averaging of the previous equation.

$$\frac{dN_m}{dt} = \frac{1}{16} K_{PA} n_a f_m f_v N_m - \Gamma_m N_m \tag{2.5}$$

From this equation we can calculate the steady state number of molecules if we know all the parameters in this equation. First we measured the photoassociation rate by measuring the number of atoms decrease during the photoassociation. There is a single atoms loss process due to off-resonant scattering of photoassociation laser. So we measured the reduction of the number of atoms with two different detunings from the excited state and the difference in the reduction of the number of atoms on resonance is the real photoassociation rate which can be see in Fig. 2.9.

$$\frac{dn_a}{dt} = K_{PA} n_a^2 - \Gamma_a n_a \tag{2.6}$$

We can integrate this spatially by assuming thermal equilibrium distribution of atoms inside a quadrupole trap.

$$\frac{dN_a}{dt} = \frac{1}{8} K_{PA} n_a N_a - \Gamma_a N_a \tag{2.7}$$

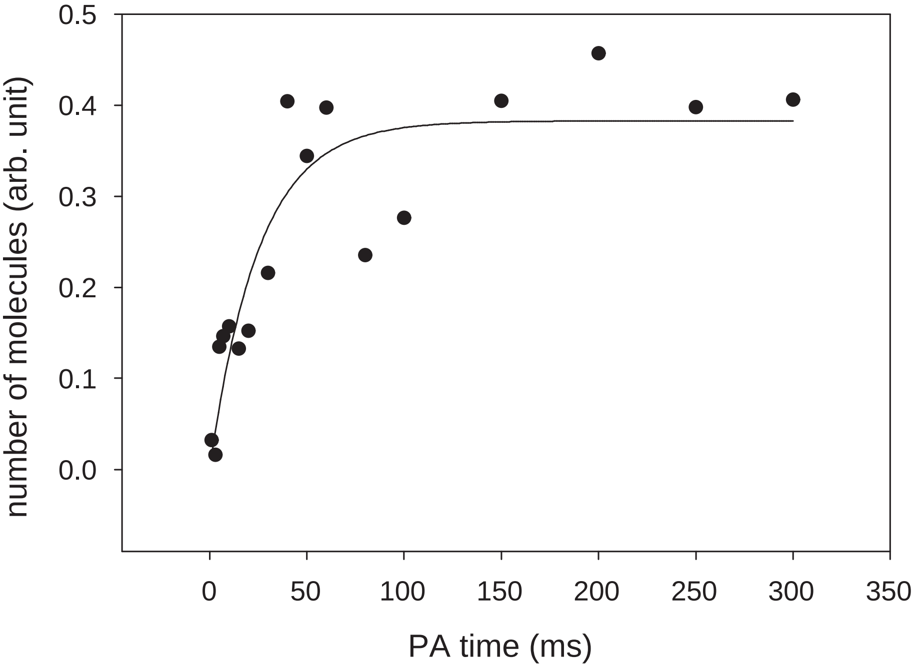

Figure 2.10: Decay rate measurement

We can use this equation to fit the data to find out the photoassociation rate.

$$\Gamma_{PA} = \frac{1}{8} K_{PA} n_a(0) = 0.0116 s^{-1} \tag{2.8}$$

The initial number of atoms we used was $N_a(0) = 8.817 \times 10^8$. To measure the decay rate of molecules during the photoassociation, we measured the number of molecules after 75ms trapping to measure the trapped molecules only as a function of a photoassociation pulse duration.

From the data shown in Fig. 2.10, we found that the decay rate of molecules is 39.53 s^{-1}. We also measured the ratio between trapped and un-trapped molecules which was 0.0997 and calculated the Franck-Condon factor between v=37 ground state vibrational level and excited state we used which is 0.321. By combining all these information the estimated number of molecules is about 4×10^3. The number of ions from the trapped molecules was counted from the channeltron signal and the detection efficiency at the typical condition is 0.2 %.

2.3.2 The estimation of the atom-molecule inelastic collision rate

As we discussed in previous section, we observed the clear difference in the decay rate of trapped molecules with and without atoms in the trap. This is the clear indication of the atom-molecule inelastic collision process in the trap. To determine this value, we measured the decay of trapped molecules with different initial atomic densities and Fig. 2.11 shows the typical decay curve of trapped molecules with atoms.

We can describe this loss process with the combination of two different loss processes which are background gas collision process and inelastic collision with atoms.

$$\frac{dn_m}{dt} = -\Gamma_0 n_m - K_{am} n_a n_m \tag{2.9}$$

(Γ_0 is background gas collision rate for molecules. n_a is atomic density. n_m is molecular density. K_{am} is the atom-molecule inelastic collision rate.)

The number of molecules is a lot smaller than the number of atoms.

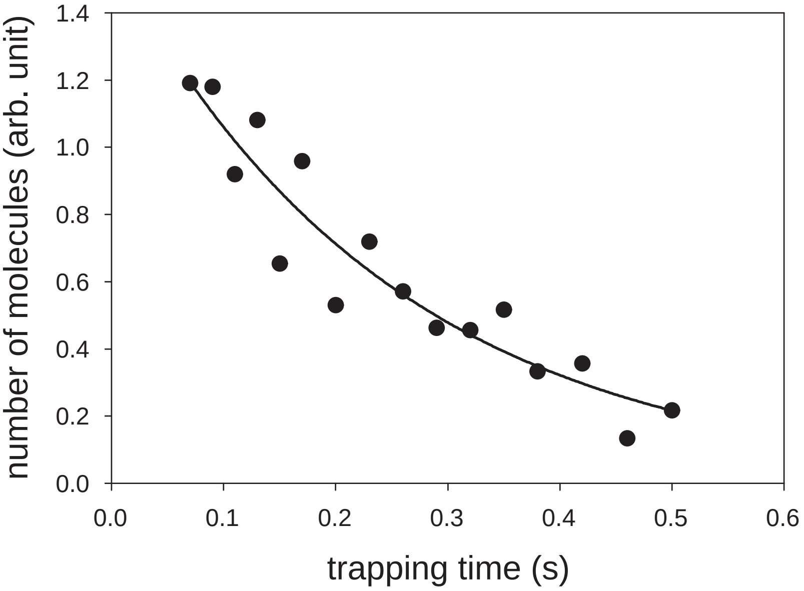

Figure 2.11: Decay of trapped molecules with atoms

Thus we can ignore the change of the number of atoms during this process. We need to know the density distributions of atoms and molecules to find out the inelastic collision rate from these data sets. By assuming thermal equilibrium, we can write down the atomic and molecular density as a function of temperature and do a spatial integration to write down the equation as a function of total number of molecules.

$$\frac{dN_m(t)}{dt} = -(\Gamma_0 + \frac{8}{27}K_{am}n_a(t))N_m \tag{2.10}$$

With measured exponential decay rates of molecules with atoms and without atoms and with the information of peak atomic density, an inelastic collision rate between atoms and molecules can be calculated. We used four

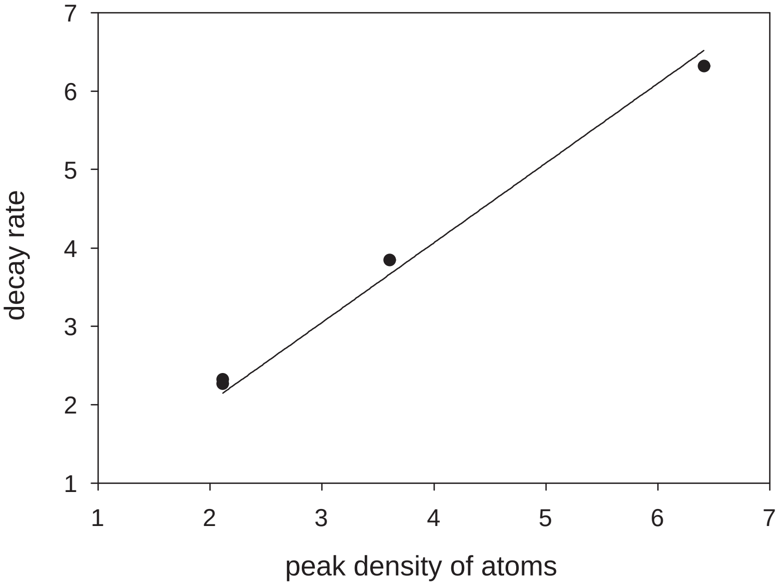

Figure 2.12: Density dependence of decay rate of molecules. Peak density of atoms is in a unit of 10^11 cm^3 and decay rate is in a unit of s^{-1}.

data sets to find out the inelastic collision rate and Fig. 2.12 shows the fitting of four data points with the equation we just derived.

From the weighted average of four measurements, we found

$$K_{am} = 3.45(\pm 0.93) \times 10^{-11} s/\mathrm{cm}^3$$

We think that the main source of the uncertainty will come from the estimation of the density of atoms and molecules. Especially molecular density depends on the molecular magnetic moment which we assumed to be one bohr magneton.

This measured value is in the same order of magnitude with measurements done by other groups and theoretical calculations [42] [43]. With the typical condition of atoms in a BEC, inelastic collisions will be the main limitation of converting atoms into molecules. If we want to have a stable ultracold molecular gas, we need to convert these high-lying vibrational level molecules into $v = 0$ molecules. One interesting proposal to do this is making molecules with two atoms per site Mott insulator. Due to the spatial separation, we can convert atoms into molecules very efficiently and possibly transfer the produced molecules into the ground vibrational level. This will be discussed in Ch.5.

Chapter 3

New BEC set-up

After the molecule trapping experiment which is described in Ch.2, we decided to build a new BEC experimental set up. Although we got some nice results from the old BEC set up, there were several major limitations in the old BEC set up. The chamber had very limited optical access and due to its big size and the necessity of putting magnetic coils inside the chamber whole experiment was not very stable. The biggest problem was the sloshing motion of a BEC which probably came from the fluctuations of magnetic trapping strength.

After considering several options, we decided to use a steel chamber with a lot of windows for a good optical access from radial directions and kept the old atomic beam slower for atomic beam source. With this new chamber, we achieved a pure Bose-Einstein condensate of 2 million ^{87}Rb atoms.

3.1 New BEC chamber

We designed our new chamber based on several objectives we had in mind for the future experiment. The first goal was to make it easy to install channeltron assembly close to the center of the chamber for the direct detection

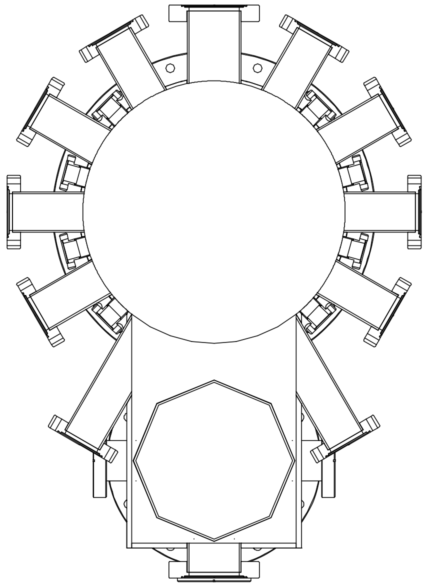

Figure 3.1: Cross-section of a BEC chamber in the radial direction

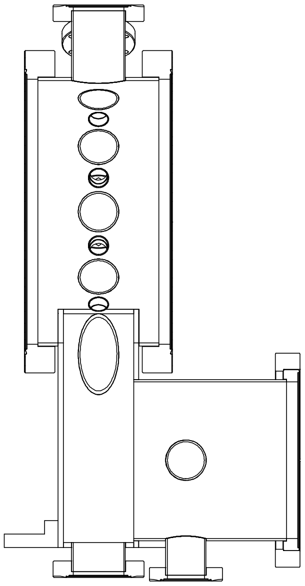

Figure 3.2: Cross-section of a BEC chamber in the axial direction

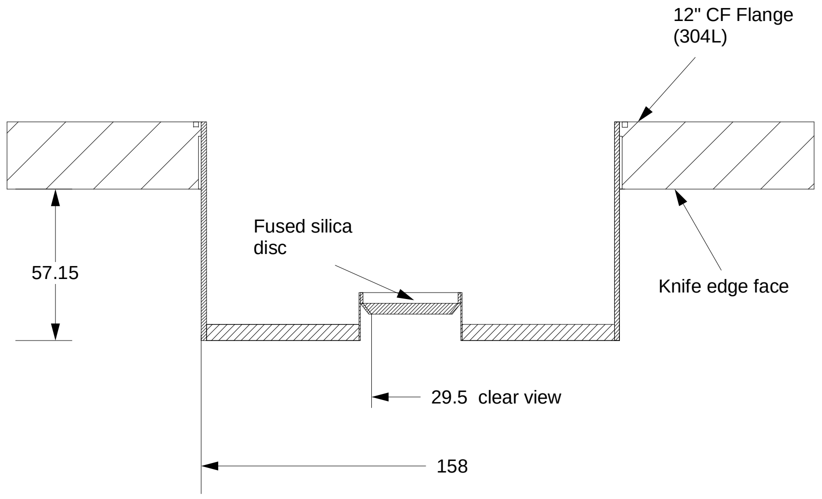

Figure 3.3: Drawing of a side flange(all unit in mm)

of molecules. It would be very difficult to make a high voltage connection and stable channeltron assembly with a glass cell chamber. This made us choose a steel chamber for our new BEC chamber.

We decided to have a pancake shape stainless steel chamber with a lot of side windows for a good optical access for a 3-D optical lattice and to use special re-entrant windows for vertical and horizontal directions for a high resolution imaging system. The lesson we had learned from the old BEC experiment was the importance of a very stable magnetic trap for the stable BEC production which will prevent a sloshing motion of the BEC cloud. We decided to put the magnetic trap coils outside of the steel chamber for the stability but to get a strong trap, it was necessary to put magnetic trap very close to the trap center. We followed the previous designs by other groups of a re-entrant well type side flange for the mounting of the magnetic trap coils.

Fig. 3.1 and Fig. 3.2 show the original design of the new BEC chamber in two different cross-sections. There are 8 small windows (one 1 1/3 inch ConFlat flange) and 10 large windows (nine 2 3/4 inch ConFlat flnages and two 3 3/8 inch ConFlat flanges) for optical access to the BEC. These windows turned out to be very good for a 3-D optical lattice set up and MOT beams. Fig. 3.3 shows the drawing for the re-entrant type side flange we used to mount magnetic trap close to the atomic cloud.

To minimize any stray magnetic field effect on the atomic cloud non magnetic stainless steel was used. We decided to use four re-entrant windows to have good optical accesses from the four vertical and horizontal directions. Re-entrant windows were constructed with special plasma bonding technique (UKAEA company in England). This special technique uses no magnetic material and this is important because any magnetic material close to the atomic cloud will affect magnetic trapping. Fig. 3.4 shows the drawing of one of the four special windows used in our experiment.

We decided to keep the previous atomic beam slower for the atomic source for the new BEC set up because our old slower was working really well. To keep horizontal imaging access open, atomic beam slower was connected at a 30 degree angle. For this we had to design a sturdy supporting structure for slower and the chamber. Fig. 3.5 shows the supporting structure for the atomic beam slower and a schematic of a new BEC set up including the chamber and Ion pump.

Due to the long evaporation time (up to 20s) needed for achieving a

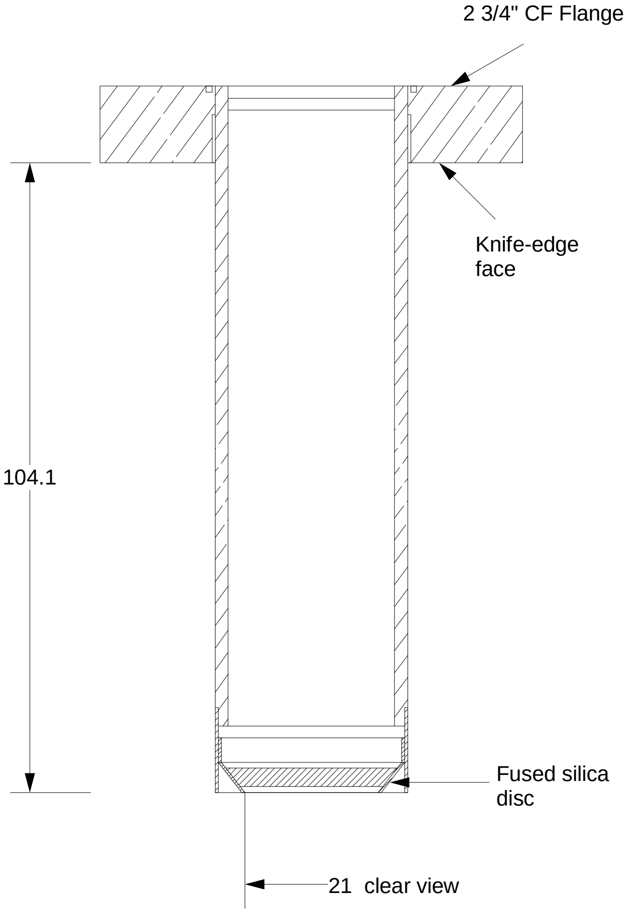

Figure 3.4: Drawing of a special window assembly for horizontal direction (all unit in mm)

BEC, the chamber should be under UHV. Usually the pressure of our BEC chamber is below 3×10^{-11} torr. To maintain this pressure, an Ion pump and a Ti sublimation pump were used. The chamber has a relatively large pumping port (6 inch diamter) toward the Ion pump (270 l/s) which makes it easier to pump down the chamber. For the initial pumping down, we used pumping station which consists of a Turbo pump and a dry roughing pump. After several days of baking out of the chamber at 200 degree, we could easily reach UHV with the Ion pump and Ti sublimation pump combination.

Another unique feature of our new BEC set up is a vertically mounted optical breadboard to have a stable mounting of optics for the experiment. We ordered a custom made optical breadboard and mounted it vertically in an optical table with a 5.5 inch distance from the center of the chamber. This strategy is working well and most of the optical mounts are much more stable in the new BEC set up.

3.2 Cloverleaf magnetic trap

3.2.1 Design of a cloverleaf magnetic trap

In the previous BEC set up, A TOP (Time-Orbiting Potential) trap was used for magnetic trapping. The rotating bias field which was used in our old set up caused many problems. The biggest problem is that due to the zero magnetic field region around the trap center which is a circle, the maximum trap volume is limited because atoms will leave the trap when they go through the zero field region slowly due to spin flips. This is sometimes

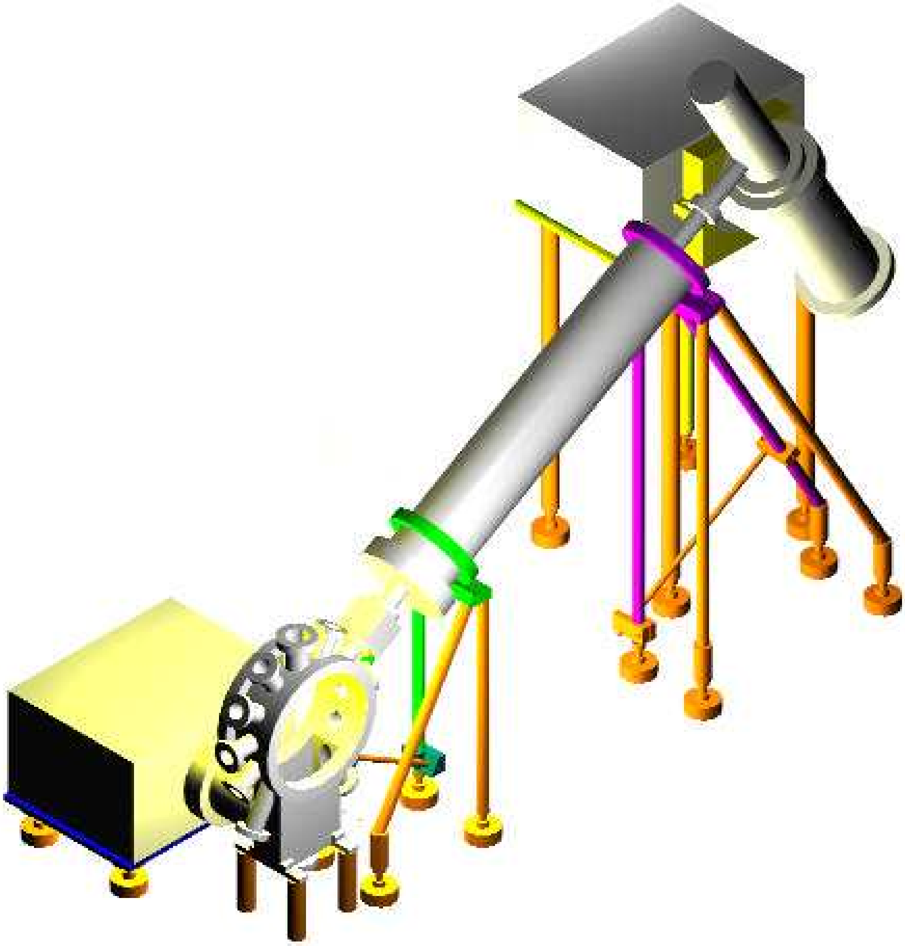

Figure 3.5: Schematic drawing of the chamber, the atomic beam slower, and the supporting structure for both.

called "death circle". This limits the maximum number of atoms in the BEC. Another problem we faced was the effect of rotating bias field on the photoassociation spectroscopy. We observed strange additional lineshapes in our photoassociation spectroscopy and it turned out that these came from the effect of rotating bias field. By considering these problems, we decided to use a cloverleaf variation of Ioffe-Pritchard magnetic trap which uses a only static magnetic field. The advantage of this variation of Ioffe-Pritchard trap is that we can have a good optical access for radial direction which is essential for a 3-D optical lattice set up. The down side of this trap is the need of using high current through coils and the proper cooling of heat generated from coils becomes very important which will be discussed later.

Magnetic field from a Ioffe-Pritchard magnetic trap configuration is determined by three parameters which are the bias field, the axial curvature, and the radial gradient.

$$|\overrightarrow{\mathrm{B}}| = \mathrm{B}_0 + \frac{1}{2}(\frac{\mathrm{B}'^2}{\mathrm{B}_0} - \frac{\mathrm{B}''}{2})\rho^2 + \frac{\mathrm{B}''}{2}z^2 \tag{3.1}$$

(B_0 : bias field, B'' : axial curvature, B' : radial gradient, ρ is the radial distance and z is the axial distance from the center of trapping coils.)

To control these three parameters independently, four coils were needed. The curvature coil is for generating the axial curvature and the cloverleaf coil is for generating the radial gradient. Curvature coil usually generates a large bias field in addition to the axial curvature. To cancel out this large bias field,

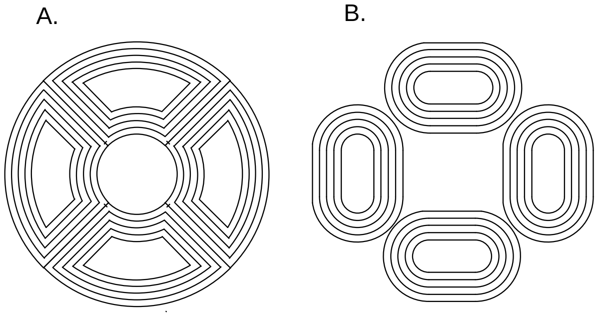

Figure 3.6: A. Cloverleaf coil shape for the magnetic field estimation B. Cloverleaf coil shape actually used for the construction of coils

an anti-bias coil is used. Because of a large bias field cancellation between the curvature coil and the anti-bias coils, it's important that these two coils are connected in series to minimize any fluctuation of the bias field coming from the current fluctuation going through coils. Because the bias field from the curvature and anti-bias coils is fixed, to control the bias field during the experiment, another extra-bias coil is needed.

With the given geometry of the chamber, the simulation of magnetic trap coils was done to find out the most effective magnetic trap coil assembly. For this simulation, a circular winding is assumed for the curvature, anti-bias, and extra-bias coils. For the cloverleaf coil, we assumed the shape in Fig. 3.6 (A). Simple Biot-Savart law was used to find out the magnetic field generated from each section of the coil and all these magnetic field contributions from many different sections were added together to find out the total magnetic field.

The criterion for the optimization was to maximize trapping frequen-

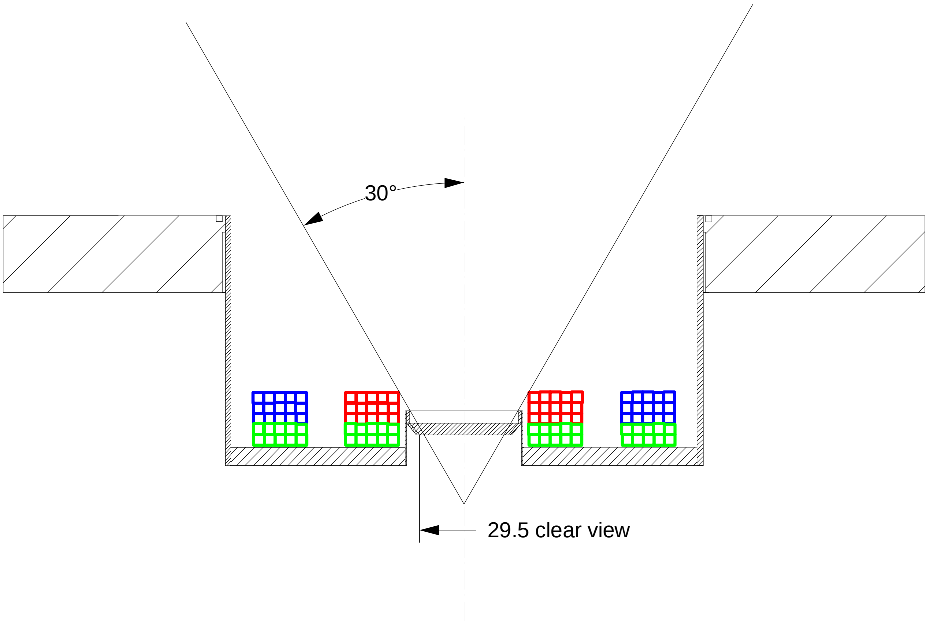

Figure 3.7: Winding and layer of magnetic trap coils.(cross-section of coils) Green : Cloverleaf coils, Red : Curvature coils, Blue : Anti-bias coils. 30 degree optical access from these windows is allowed which will be important in future applications which require more laser beams.

cies with a fixed total power consumption by the magnetic trap coils. The optimum windings and layers of coils were found after trying many different combinations. Fig. 3.7 shows the final optimized winding and layer of various coils. Cloverleaf coils and curvature coils are close to the trap center and anti-bias and extra-bias coils are located further from the center to make a constant bias field without affecting curvature or gradient of the magnetic trap. Each coil had five windings and except the cloverleaf coil which has two layers, all other coils have three layers.

3.2.2 Construction of the magnetic trap

Because of the easiness of stacking, square copper tubing was used for our magnetic trap coils. We used 1/8 inch diameter square copper tubing which has an inner diameter of 0.61 inch. We used fiber insulation to insulate the copper tubing. Due to the thickness of the tubing, we cannot wind it according to the assumed shape of cloverleaf coil. We chose an oval shape cloverleaf coil which is shown in Fig. 3.6(B). There was a small change in the measured radial gradient due to the change in the shape of the cloverleaf coil which will be discussed in the next section.

Another important aspect of the magnetic trap construction is the consideration of the water cooling capacity. We should be able to run the required current through the coils without heating them too much. Depending on the heat generation, it was necessary to divide some of the coils into two separate coils with separate water cooling connections. For the cloverleaf coil all four coils in one side were connected electronically in series but water cooling connection to each coil was separated. Curvature and anti-bias coils had to be constructed with two separate pairs to increase the water cooling effectiveness. In other words, each coil was connected in series for electrical connection but water cooling connection was parallel to increase the total flow rate with given the pressure of water system.

To have a very stable magnetic trap configuration, after the construction of the magnetic trap, magnetic trap coils were glued together and mounted inside the well of the side flange. The mount for the various leads going in and out of the magnetic trap were securely installed on the side flange.

3.2.3 Test of the magnetic trap

Before starting the experiment, the magnetic field generated from the magnetic trap coils was measured with a Hall probe inside the chamber which was not yet under vacuum at the location of the atomic cloud. The radial gradient from the cloverleaf coils, the axial curvature from curvature coils, and the bias field from curvature and anti-bias coils were measured.

The gradient along the radial direction at 200A current through cloverleaf coils was 75.07 G/cm which was only 77 % of the calculated value but this difference was expected because of the change we made in the design of coil which was mentioned earlier. The measured curvature turned out to be 175G/cm^2 at 400A current through the pinch coil which was 84 % of theoretical value and we found that this was coming from slight difference in the distance between coils of the actual trapping coils from the value we used for the simulation.

The magnitude of bias field is very important in determining the radial trapping frequency. The measured bias field from pinch and anti-bias coils was -3.67 G at 375 A. The bias field from extra bias coil was 0.955 G per 1 A.

With 500 A current going through cloverleaf coils and 375 A current going through curvature and anti-bias coils, we could achieve trapping frequencies of 170.5 Hz for the radial direction (with 1G bias field) and 11.6 Hz for the axial direction. These are reasonable trapping frequencies to make a

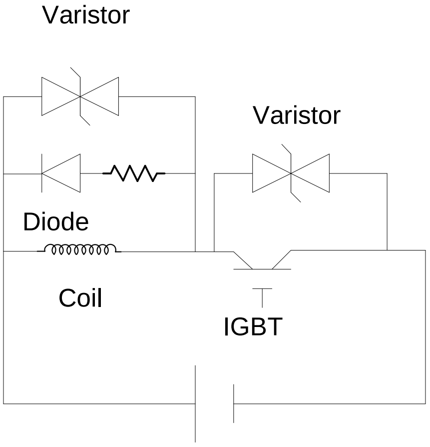

Figure 3.8: Protection circuit for IGBT switches

BEC. Lambda EMI power supplies (model ESS 30-500 for the cloverleaf coils, model ESS 40-375 for pinch and anti-bias coils, and EMS 10-200 for extra-bias coils) were used for the magnetic trap.

3.2.4 IGBT switches for current control

To control the flow of current in each coil, IGBT (Insulaed Gate Bipolar Transistor) switches are used.

Fig. 3.8 shows the typical circuit we used for IGBT switch. Proper protection circuit was needed to prevent high voltage spike when the switch was turned off. When the switch is off, the current will flow in protection circuit which is made of a diode and a resistor which will dissipate the power without the voltage spike across the IGBT switch. Varistors are used for further protection of IGBT switches. A few different resistors and varistors are used depending on the current flowing. For I=375 A pinch and anti-bias

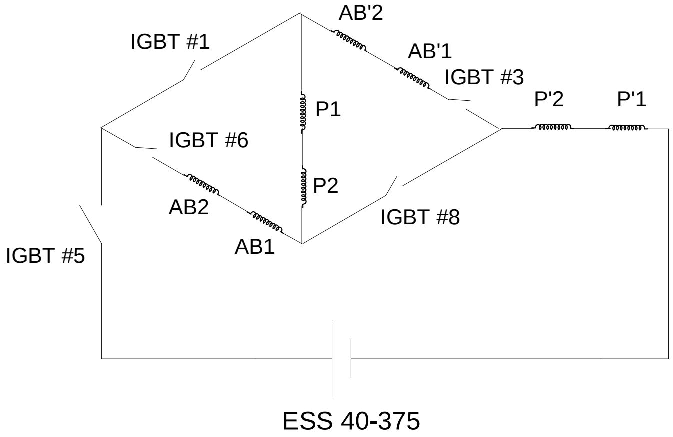

Figure 3.9: Anti Bias and pinch coils connection with IGBT switches

coils, we used 1Ω resistor and clamp volage of 345 V varistor.

For cloverleaf coil one switch (POWEREX model : CM1000HA-28H) was used to turn on and off the all eight coils and for extra bias coil one switch (POWEREX model : CM600HA-24H) also was used to turn on and off two coils. A little complicated switching diagram was used for pinch and anti bias coils because pinch coil was also used as a MOT magnetic coil.

Five IGBT's (POWEREX model : CM600HA-24H) were used to control the current going through pinch and anti bias coils as depicted in Fig. 3.9. By controlling switches, a MOT magnetic coil configuration or a magnetic trap coil configuration can be chosen depending on the sequence of the experiment. The reason we chose to use a pinch coil for our MOT magnetic coil will be explained in a later section. In MOT configuration, IGBT 1 and IGBT 8 are closed and IGBT 6 and IGBT 3 are open to make current go through pinch coils only. In magnetic trap configuration, IGBT 1 and IGBT 8 are open and

IGBT 6 and IGBT 3 are closed to make current go through anti-bias coils and pinch coils.

3.2.5 Water cooling system

More than 30 kW power needs to be dissipated through water cooling to prevent the melting of the magnetic trap coils. The calculated necessary flow rate for our trapping coils to limit the temperature increase of the water to less than 10 degree C was about 9 gallon/min and because of the small size of the copper tubing we used, inlet pressure needed to be more than 100 psi to get the required flow rate. A closed loop water cooling system with a heat exchanger with building chilled water to cool the internal cooling water was used to cool magnetic trap coils. This system has enough flow rate but the maximum pressure was only 60 psi. A booster pump was installed to increase the pressure up to 110 psi. With this new combined cooling system, the temperature increase of the coils was less than 10 degree C. To prevent any damage from a malfunction of the cooling system, we installed interlock switches for temperature and flow rate of water at outlet side. In the case of abnormal increase of temperature or decrease of flow rate, these interlock switches will shut down power supplies automatically to prevent the melting of coils.

Another improvement we made for our new BEC set up was to install water temperature servo loop which has integral and proportional gain compared to the previous servo loop which has only a proportional gain to maintain a stable water temperature during the experiment. It turned out that the combined bias field of the magnetic trap was quite sensitive to the small change of cooling water temperature and it was essential to have a stable water temperature to have a stable production of a BEC with same number of atoms. We cannot maintain the temperature of cooling water at the fixed temperature all the time due to the change of heat load during the cycle of the experiment and the large volume of cooling water. But after 30 minutes cycling of the experiments, temperature will cycle with the same period of the experiment and this will make the bias field very stable for the stable production of a BEC.

3.3 Laser systems for the experiment

To have a MOT (Magneto Optical Trap), we need many laser beams with different frequencies. Fig. 3.10 shows the laser frequencies we need for the operation of a MOT. Actual details of the operation principle of a MOT is available now in many review articles and books [2]. Like all alkali metal elements, ^{87}Rb has two ground state hyperfine states F=1 and F=2. We use a transition from F=2 ground state to F=3 excited state for the MOT trapping laser. A repumper laser which is resonant with the transition from F=1 ground state to F=2 excited state is needed to keep the cooling cycle closed. A slower beams is used to slow down atoms in the Zeeman atomic beam slower and a probe beam is used for the imaging of the atomic cloud. A depopulator is used for the dark MOT which will be explained later. Except the repumper laser

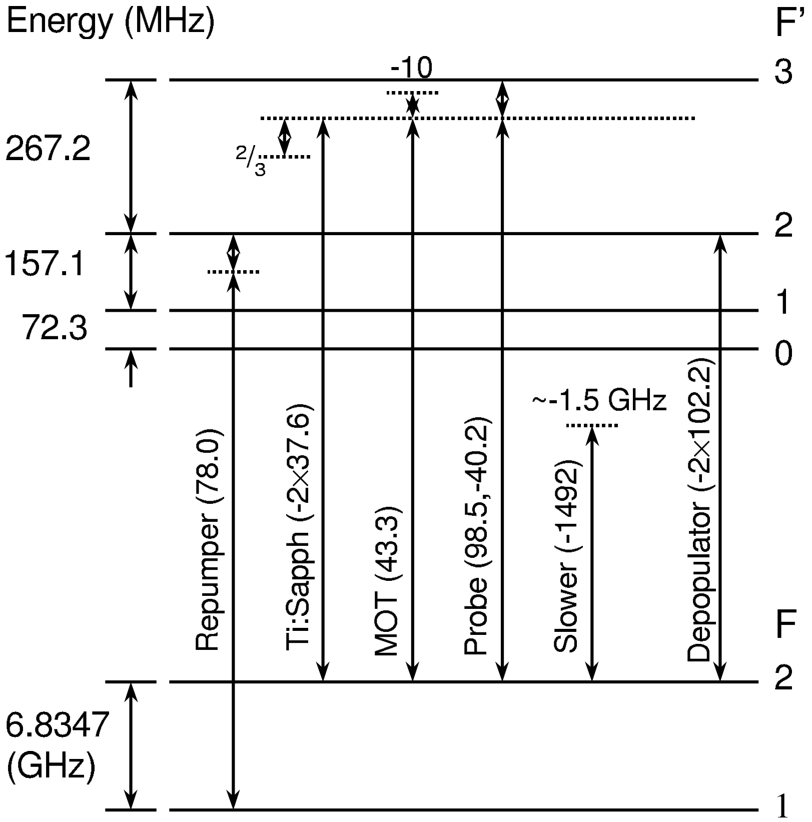

Figure 3.10: Various laser frequencies which we need for a MOT

beams, all beams are for F=2 ground state. Due to the big hyperfine splitting between F=1 and F=2 hyperfine state, we decided to use separate lasers for F=1 state and for F=2 state.

We used a Ti-sapphire laser (Coherent model : MBR110) pumped by Nd:YAG solid state laser from (Coherent model : Verdi-10) to produce the laser beams for F=2 state which are MOT beams, the probe beam, the slower beam, and the depopulator beam . We used a standard Lamb-dip locking set up to stabilize the frequency of the MBR110 laser. We have separate optical tables for the BEC chamber and lasers. To transfer the laser beams between two tables, optical fibers were used. This method has the advantage of separating the alignment of the laser system and the experiment. Also after the optical fiber, alignment is very stable and the beam quality is also very good. At the experimental table, the main beam was split into many different beams with different frequencies. AOM's (Acoustic Optical Modulator) were used to shift the frequencies of the laser beams and also power was controlled with an analog voltage input into an AOM's.

Fig. 3.11 and Fig. 3.12 shows the actual scheme we used to split the main beam into various beams with different frequencies and one of the main changes we made in this new set-up was using 6 beam configuration for the MOT. This 6 beam configuration reduced the effect of absorption by the atoms and improved the number of atoms trapped in the MOT. The diameter of each MOT beam is 3 cm and power per each beam is 33 mW.

We used a master and slave diode laser system for the remper beams.

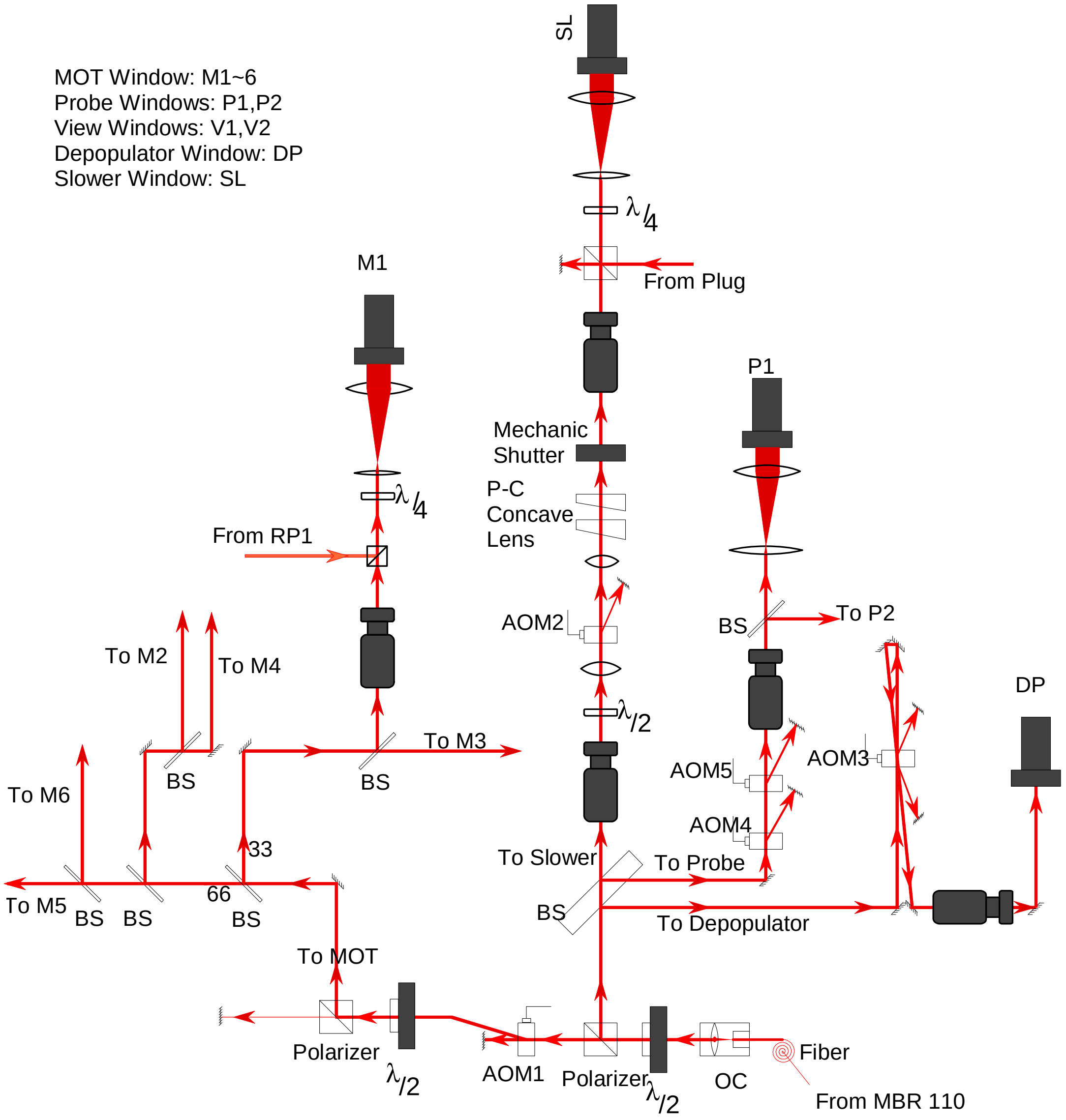

Figure 3.11: Optics set up in the experiment optical table

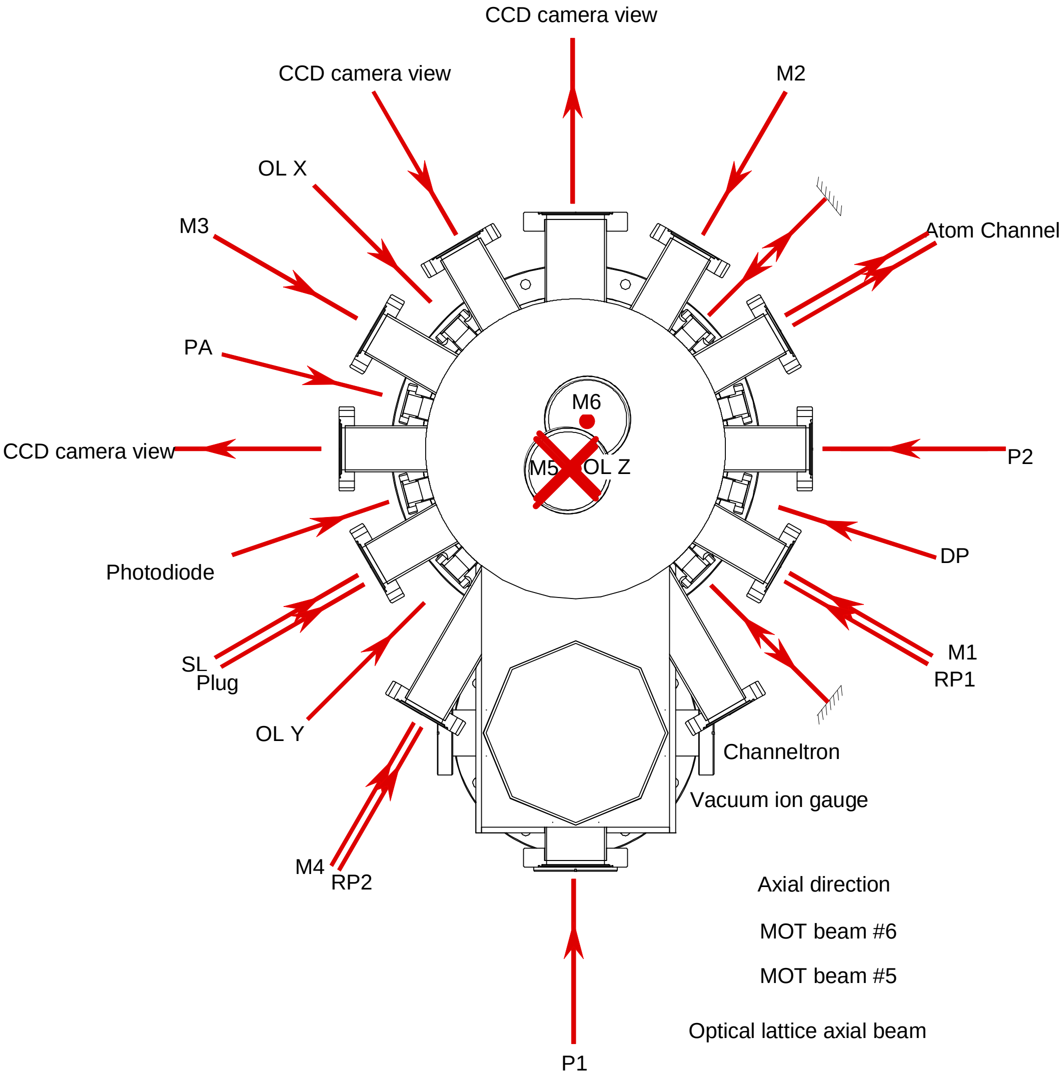

Figure 3.12: Laser beams arrangement

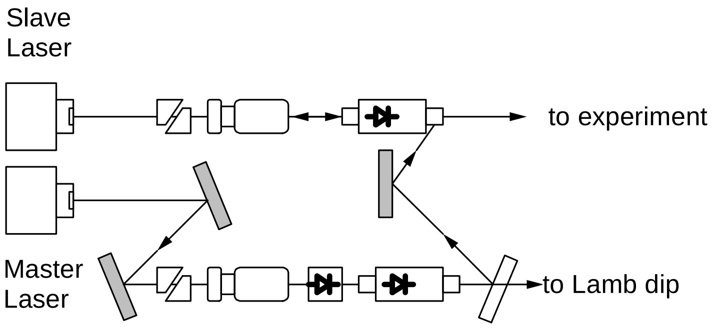

Figure 3.13: Master and slave diode laser set up for repumper beams.

For the master diode laser, DBR diode laser (Sanyo) was used. Frequency of this laser can be tuned easily by varying the current for the grating section. Due to the limited power (5 mW) from this laser, injection locked slave diode laser (Sanyo 50 mW laser diode) was used for the repumper laser. Fig. 3.13 shows the schematic of this set up.

The frequency of the repupmper laser was stabilized with a standard Lamb-dip set up with feedback into the grating section current for the DBR master laser. The laser beam was transferred to the experiment table using an optical fiber and on the experimental table the laser beam was split into a plug beam and repumper beams. This splitting is for the implementation of a forced dark MOT which will be discussed in the next section. Repumper beams have a hollow region at the center which was generated by imaging a dark spot into the center of the chamber. 1 mm diameter dark spot on the window was 10 times magnified at the center of the chamber. Two identical rempumper beams were used in orthogonal directions and these beams were combined with MOT beams using polarizing beam splitting cube as shown in

Fig. 3.11. The plug beam was used to plug this hole when we don't need a dark MOT and this plug beam was combined with the slower beam.

3.4 RF coil and channeltron assemblies

The final stage of making a BEC is to use a RF field to cool atoms with evaporative cooling. Because our chamber is made of stainless steel, the RF coil had to be inside the chamber. Typically a few hundred mG of RF field is needed for the evaporative cooling. Also RF coils inside should not block laser beams going through the chamber. With these conditions in mind, RF coil set up was designed. We used 22 gauge copper wire with Kapton film insulation from ISI (model : KAP2). Two identical square loops were used for RF field generation. The coils were mounted on the holders welded to one of the side flanges. This flange has two 1 1/3 inch feedthroughs providing electrical connection to the RF coils. Fig. 3.14 shows the assembled RF coil set up.

We measured the RF field generated from coils inside the chamber with a small circular pick up coil as a function of frequency. Fig. 3.15 shows the result of this measurement. With fixed input power, there was a variation of the magnetic field from RF and this came from the difference of RF coil impedance which is a function of frequency.

This variation of impedance made it necessary to control the power and speed of RF ramping down during the evaporation. We used a function generator from Rohde & Schwarz (model : SMH) as a RF source and a GPIB

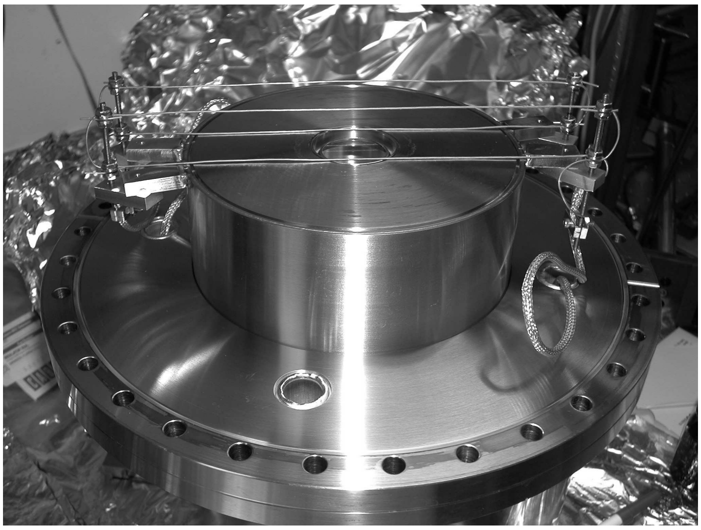

Figure 3.14: Picture of a RF coil assembly

connection was used to control the power and frequency of RF field.

Channeltron is an ion detector which was used in the previous molecule formation and trapping experiment. We decided to install a channeltron in our new chamber too. A bigger size from Sjuts (25mm diameter, model : KBL25RS) was used in the new BEC set up to increase the efficiency of ion detection. To install the channeltron inside the chamber, we designed a compact and rigid structure with high voltage connection. Fig. 3.16 shows the channeltron assembly before we put it inside the chamber.

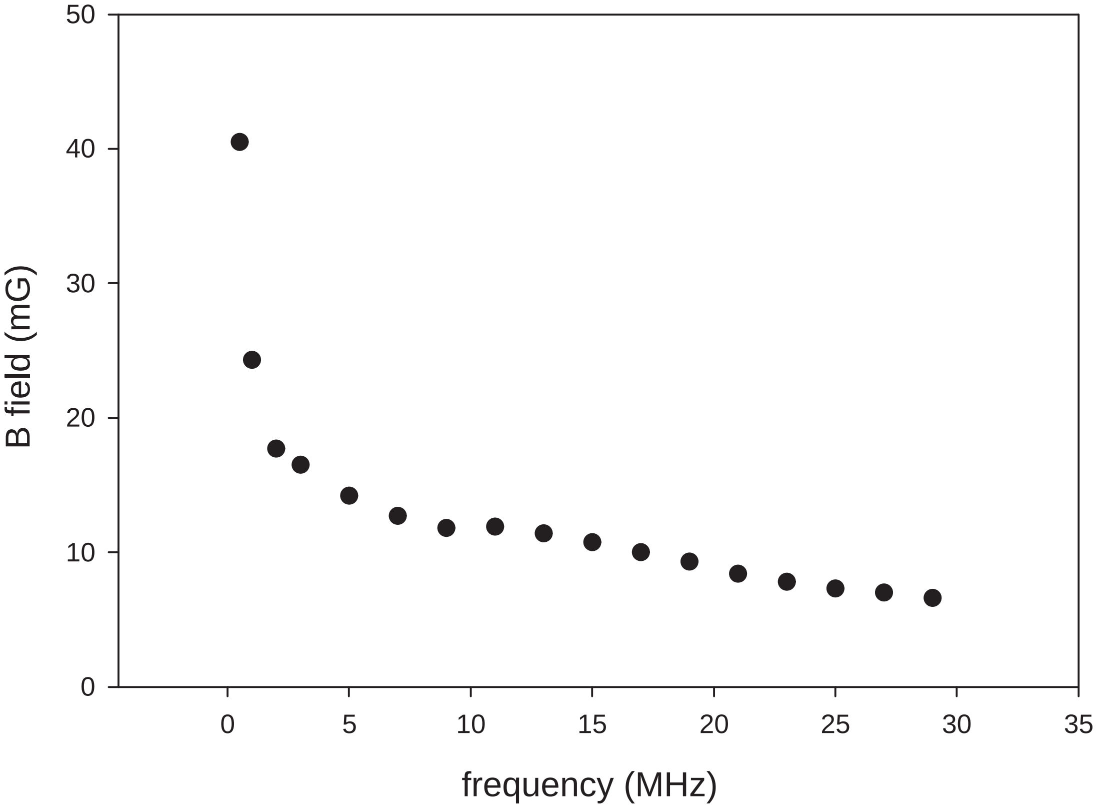

Figure 3.15: Test of a RF coil inside the chamber at 10 mW input power

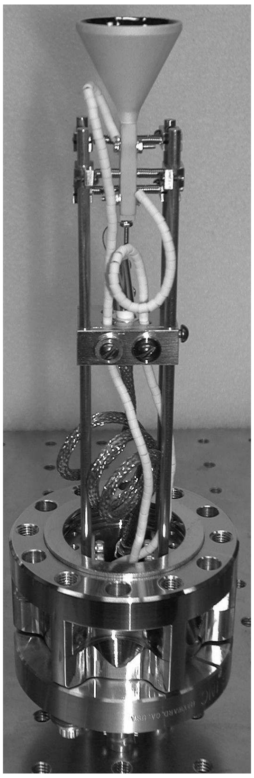

Figure 3.16: Picture of a channeltron assembly

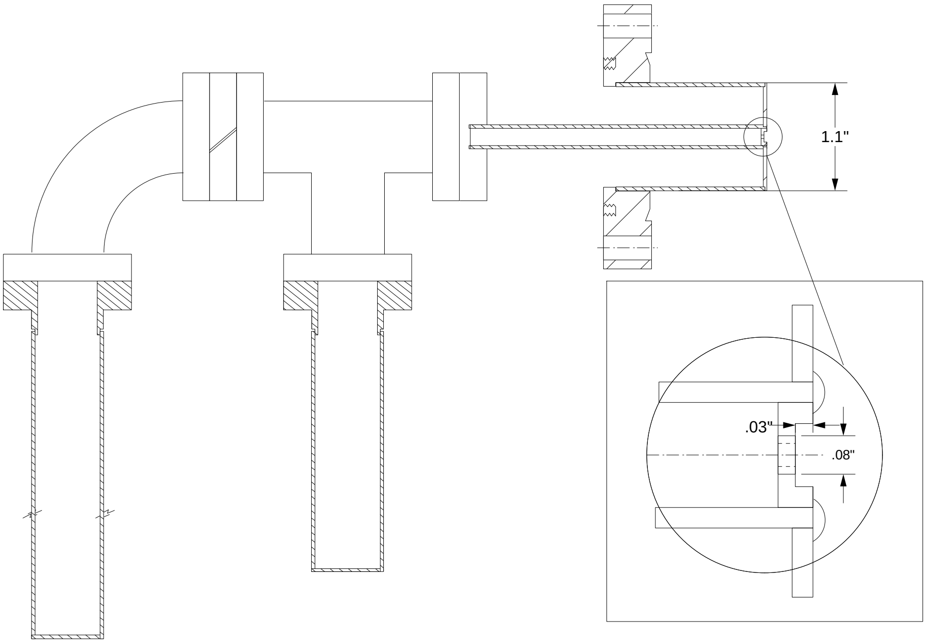

Figure 3.17: Drawing of a new oven

3.5 Experimental sequence toward the BEC

3.5.1 MOT(Magneto-Optical trap)and dark MOT

An atomic beam slower was used to load atoms into the MOT (Magneto-Optical Trap). A new oven was installed in the slower as a source of hot Rb atoms. Fig. 3.17 shows the drawing of the new oven. This oven was designed to be used as a source for two different atomic species. Possible future plan is to use Li and Rb as our dual species oven elements and doing experiment with Li-Rb mixture atomic gas. Right now only Rb oven part is being used. The temperature of the oven is maintained at 200 degree and at this temperature estimated beam intensity going into slower is 7.6×10^{11}atoms/s cm^2.

As described in a previous section, we used 6 beams configuration for

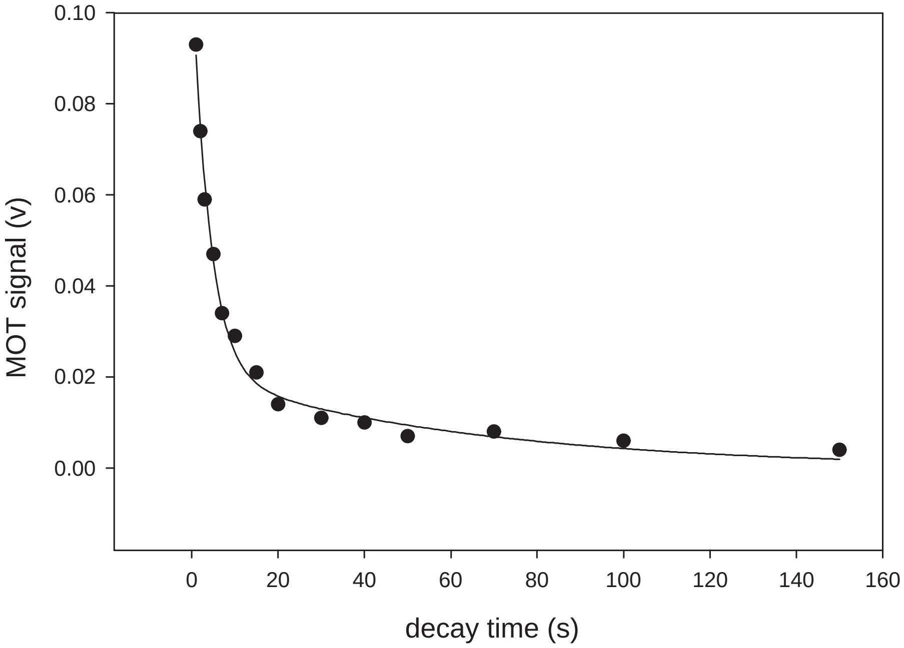

Figure 3.18: Dark MOT decay curve

the MOT to increase the number of atoms which can be trapped in the MOT. Fig. 3.19 shows the loading curve of the MOT. We can get about 5×10^9 atoms in our MOT with 20-30 second loading time and after loading is complete, atoms in the MOT are transferred to a forced dark MOT which was briefly describe in Ch.2. A forced dark MOT is a well established technique to increase the density of atoms by minimizing the time the atoms spend in the F=2 state. For Rb an additional depopulator beam which actually pumps atoms into the F=1 (dark state) state is needed for the dark MOT. Fig. 3.18 shows the decay curve of a forced dark MOT.

There is a fast initial decay in the dark MOT and we found that loading atoms directly into the dark MOT produces a much fewer number of atoms

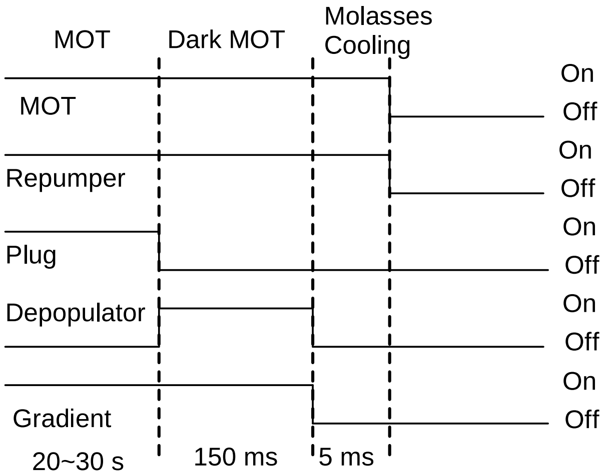

Figure 3.19: MOT loading curve

compared to the method of loading atoms into the MOT and transferring them into a dark MOT. We used usually 150 ms dark MOT duration which gives us the best density and temperature combination without loss of atoms. Typical density of atoms in a dark MOT is 2×10^{11} cm^{-3} and temperature of atoms is 182 μK.

After a forced dark MOT period, a dark Molasses cooling where we turned off the MOT coils and leave MOT beams on was used to further reduce the temperature of atoms. With -35 MHz detuning and a reduced power of MOT beams, the temperature of the atoms was reduced to 47 μ K with a density of 8.5×10^{10}cm^{-3} after 5 ms cooling.

Finally Fig. 3.19 shows the whole sequence of preparing atoms for the magnetic trap.

3.5.2 Magnetic trap

As described in a previous section, Cloverleaf type variation of Ioffe-Pritchard magnetic trap was used to trap atoms after molasses cooling. Magnetic trap was turned on suddenly after all laser beams were turned off. Careful optimization of magnetic trapping parameters was necessary to minimize any loss of atoms or decrease in phase space density. To maintain the phase space density, the equilibrium size of trapped cloud should be similar to the cloud size before the magnetic trapping. If the trap is too shallow, the density of atoms will decrease and if the trap is too steep, the temperature of atoms will increase. And both cases will decrease the phase space density of atoms. With the temperature and density of atoms after the molasses cooling, magnetic trap frequency should be around 9 Hz for a mode-matched transfer. The maximum trapping frequencies are 11.6 Hz for the axial direction and 170.5 Hz for the radial direction. With a reduced current in the curvature coil, axial trapping frequency can be reduced. For the radial direction, there are two ways of reducing the trapping frequency. One is changing the current for the cloverleaf coil to change the radial gradient and the other is changing the current for the extra-bias coil to change the bias field. However, Ioffe-Pritchard type magnetic traps have the point of instability [5], so the best way to control radial trapping frequency is to increase or to decrease the bias field by changing the current going through the extra-bias coil.

After we transfer the atoms to the magnetic trap, we adiabatically increase the trap strength to the maximum to maximize the elastic scattering

Magnetic trap steps	Capture	Compression	Evaporation	Decompression
Cloverleaf coil current (A)	500	500	500	500
Pinch coil current (A)	330	330 → 375	375	375
Extra bias coil current (A)	155	155 → 7.5	7.5	7.5 → 55
duration (s)	1	2	20	0.1

Table 3.1: The parameters and sequence used in the magnetic trapping

rate for the evaporation. Firstly a current for the curvature coil is increased to the maximum and then the current for extra-bias coil is reduced to increase the radial trapping frequency. There are a few technical difficulties we experienced for the initial magnetic trapping process. The first difficulty was the exact alignment of each magnetic coil. Initially, we used an extra-bias coil for the MOT but we found that the center of cloud in the MOT is different from the center of the cloud at magnetic trap by a significant amount(1-2mm). This difference caused heating of the cloud during magnetic trapping. We decided to use the curvature coil for the MOT coil and this solved the problem. Another problem was the existence of radial bias field from curvature and anti-bias coils. There was a change of a radial position of the BEC depending on the current of curvature and anti-bias coils.

Fig. 3.20 shows the result of this measurement and from the linear fitting the radial bias field at curvature current of 375 A is 17.9 G.

3.5.3 Evaporative cooling

To cool atoms further, magnetic field dependence of the RF transition frequency between different zeeman levels was used to selectively remove

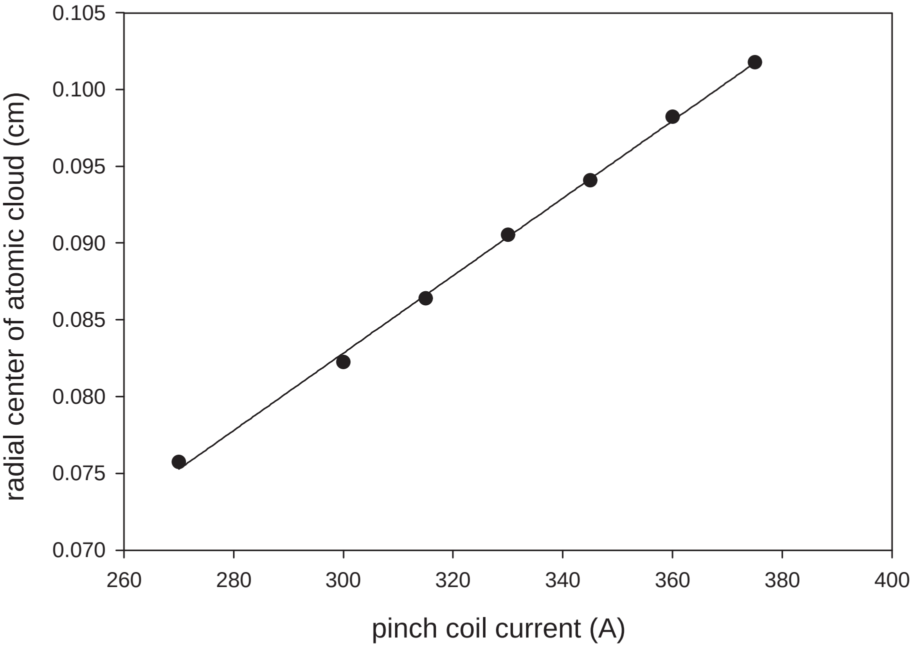

Figure 3.20: Radial displacement of trapped atoms due to the radial bias field

atoms with higher energy than the average energy. After removal of atoms with a higher energy, remaining atoms rethermalize into a lower temperature. By continuously decreasing the RF frequency, the temperature can be reduced and density of atoms will be increased until the BEC transition. To optimize this evaporative cooling process, whole process was divided into four sub sequences and the RF power and speed of RF ramping down in each sequence was optimized to maximize the final number of atoms in a BEC.

Tab. 3.2 shows the current experiment sequence of evaporation. Although we tried to optimize the process, there seems to be some more room for the improvement. Especially, because of the role of inelastic collisions, it may be helpful to reduce the trap frequencies during the evaporation.

Evaporation steps	1	2	3	4
Start frequency (MHz)	30	10	2	1.4
End frequency (MHz)	10	2	1.4	1.1
Power (dBm)	-32	-35.5	-40	-42
duration (s)	10	4	3	3

Table 3.2: The parameters used in the evaporative cooling process to achieve a BEC. Power setting was for the function generator and there is a RF amplifier with the typical gain of 53 dB. Also RF divider was to generate two identical RF signals into RF coils.

After evaporation, we turned off the magnetic trap suddenly and used a standard TOF (Time Of Flight) absorption image to get the information about the number and temperature of the BEC.

3.5.4 Imaging of the BEC

Our BEC set up allows us to take an image of the BEC cloud along the horizontal or vertical directions. For most of the pictures, the horizontal direction was used. Our imaging set up consists of two achromat lenses. One has a focal length of 25 cm and the other has a focal length of 40 cm. The magnification was calibrated by measuring the free fall of the cloud. For the fitting of the cloud, a Castin-Dum theory of an expanding BEC was used. Fig. 3.21 and Fig. 3.22 show the typical example of our TOF pictures of the BEC. The bimodal distribution of the expanded BEC with a clear difference from a isotopic thermal cloud can be seen.

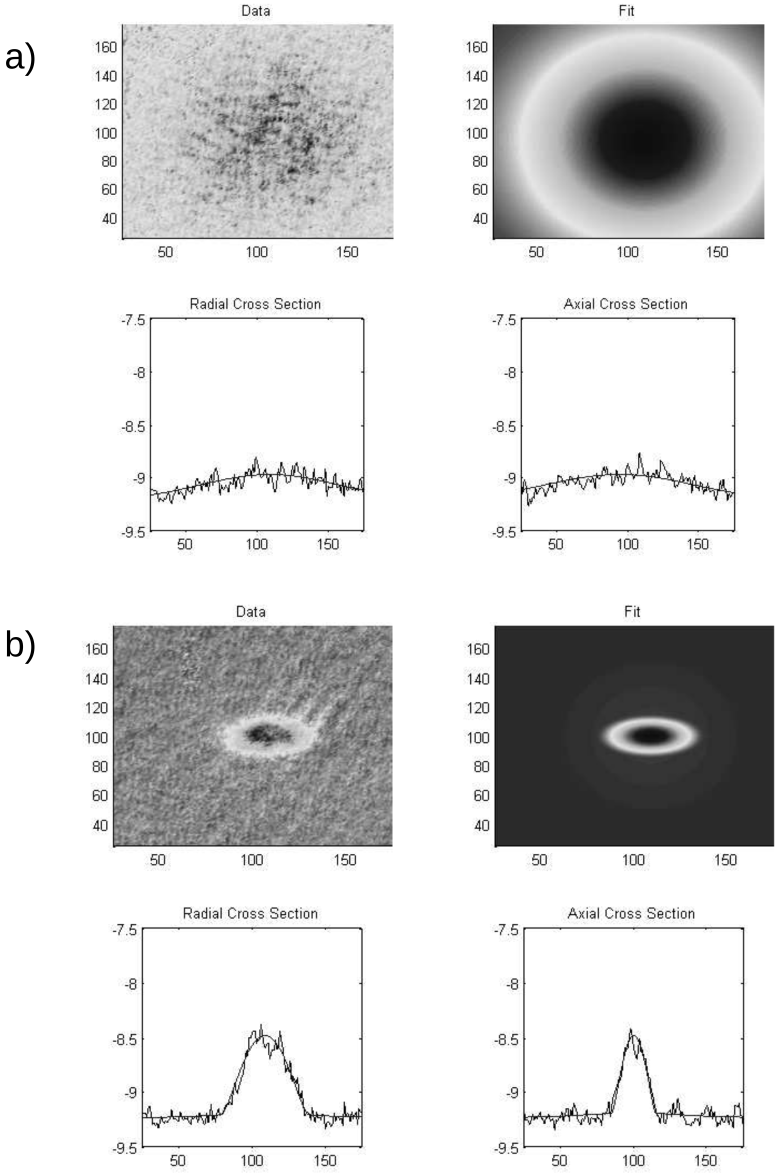

Figure 3.21: TOF BEC images with fitting. a) Final RF = 1.1 MHz, $N = 1.1 \times 10^7$, T = 755nK, condensate fraction =0.0, b)Final RF = 0.96 MHz, $N = 7.2 \times 10^6$, T = 554nK, condensate fraction =0.13.

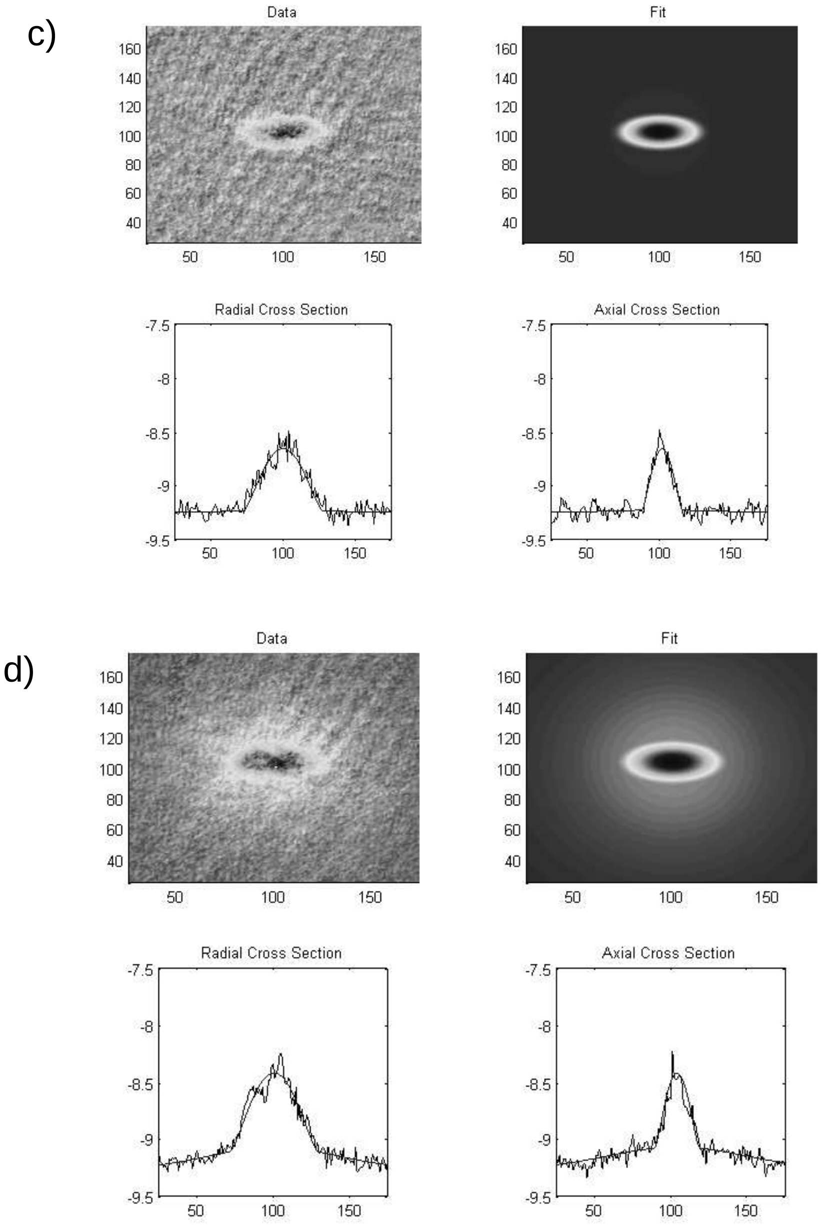

Figure 3.22: TOF BEC images with fitting. c)Final RF = 0.92 MHz, $N = 1.7 \times 10^6$, $T = 258$nK, condensate fraction =0.63, d)Final RF = 0.89 MHz, $N = 0.92 \times 10^6$, $T = 169$nK, condensate fraction =0.80.

Chapter 4

Quantum phase transition with ultracold atoms

A Quantum phase transition is a phase transition driven by quantum fluctuations at T=0 instead of thermal fluctuations [44]. Many experiments and theoretical work on the quantum phase transition have been focused on condensed matter systems. But recently realized system of ultracold atoms in an optical lattice presents us the most ideal system to study a quantum phase transition.

4.1 Ultracold atoms in an optical lattice

4.1.1 Quantum phase transition from a Bose-Hubbard model

One of the simplest systems which predicts quantum phase transition is the Bose-Hubbard model.

$$H = -J \sum_i (a_i^\dagger a_{i+1} + a_{i+1}^\dagger a_i) - \mu \sum_i n_i + \frac{1}{2} U \sum_i n_i (n_i - 1) \tag{4.1}$$

where $a_i^\dagger$ is the bosonic creation operator and a_i is the bosonic annihilation operator at site i and n_i is the bosonic number operator at site i. J is the hopping term between neighboring lattice sites. U is the on-site interaction energy at each lattice site and μ is the chemical potential which fixes the number of particles in the system. The first careful study of a phase diagram of this system was done by Fischer [45]. The qualitative understanding of many body ground state can be obtained by considering two extreme cases. At zero tunnelling rate between different lattice sites, the system tries to minimize the energy at each lattice site which is $-\mu n_i + \frac{1}{2}Un_i(n_i - 1)$. It can be easily shown that there is a simple relation between n_i and $\frac{\mu}{U}$. Each lattice site in the interval $n - 1 < \frac{\mu}{U} < n$ will have n bosons. In other words, with zero tunnelling, the many body ground state becomes a Fock state where each lattice site will have exactly same number of atoms. There is a big energy penalty for a boson to hop to another lattice site and this is still true at finite tunnelling rate. This energy gap to all excitations is a very important property of the Mott insulator. But at some point, the tunnelling between different lattice sites will be energetically possible and the system will become a superfluid. In other words, if energy gap to excitations decreases to zero, a superfluid state will emerge. This process can be modelled with mean field approximation and a ground state phase diagram can be obtained with this analysis.

There are several rigorous simulations to confirm the basic picture of this phase diagram [46] [47]. This shows that there is a quantum phase transition from a superfluid to a Mott insulator at T=0. Bosons in this model can represent cooper pairs in Josephson junction arrays [48] or helium atoms in a porous media [49]. There were experiments with these systems to study a quantum phase transition from a superfluid to a Mott insulator.

4.1.2 Ultracold atoms in an optical lattice as a realization of the Bose-Hubbard model

It was first suggested by D. Jaksch et al. [28] that a Bose-Hubbard hamiltonian can be realized with ultracold atoms in an optical lattice. The most general description of ultracold atoms in an optical lattice can be given with field operator expression of the hamiltonian.

$$H = \int d^3x\psi^\dagger(x)(-\frac{\hbar^2}{2m}\bigtriangledown^2+V_0(x)+V_T(x))\psi(x)+\frac{1}{2}\frac{4\pi a_s\hbar^2}{m}\int d^3x\psi^\dagger(x)\psi^\dagger(x)\psi(x)\psi(x) \tag{4.2}$$

($\psi(x)$ is a boson field operator for atoms in an optical lattice, $V_0(x)$ is the optical lattice potential, $V_T(x)$ is an additional trapping potential, and a_s is a s-wave scattering length.)

A 3-D optical lattice can be formed by three orthogonal standing waves and if the three beams have orthogonal polarizations, the optical lattice potential can be written as

$$V_0(x) = V_0\sum_i \sin^2(k_i x_i) \tag{4.3}$$

With a periodic potential, a single particle state will be a superposition of Bloch states and with appropriate choices, well localized Wannier function can be constructed. Then boson field operator can be written.

$$\psi(x) = \sum_i b_i w(x - x_i)$$

(b_i is the annihilation operator and $w(x - x_i)$ is the Wannier function for i lattice site.)

With this expansion, the original hamiltonian can be written again.

$$H = -J \sum_{<i,j>} b_i^\dagger b_j + \sum_i \epsilon_i n_i + \frac{1}{2} U \sum_i n_i(n_i - 1) \tag{4.4}$$

(n_i is the number operator at site i.)

The parameter $U = \frac{4\pi a_s \hbar^2}{m} \int d^3x |w(x)|^4$ corresponds to the on site interaction energy between atoms. $J = \int d^3x w^*(x - x_i)[-\frac{\hbar^2}{2m} \bigtriangledown^2 + V_0(x)] w(x - x_j)$ is the hopping matrix element between adjacent sites. $\epsilon_i = \int d^3x V_T(x) |w(x - x_i)|^2$ is an energy offset of each lattice site. This transformation shows that a Bose-Hubbard hamiltonian can be obtained from the system of ultracold atoms in an optical lattice.

With the given optical lattice potential and external trapping potential, Wanier functions can be calculated and these can be used to calculate parameters of Bose-Hubbard hamiltonian. This shows the complete control of parameters in a Bose-Hubbard model by using ultracold atoms in an optical lattice. Also there is a very small impurity in this system and in fact there is a theoretical proposal to create a perfect atomic crystal [59]. This is a clear advantage over the condensed matter systems which usually cannot avoid impurities in them.

Another advantage of an atomic system is its ability to detect various properties of the system easily. Absorption imaging technique can be used to detect the spatial distribution of atoms and with a TOF (Time Of Fight) the momentum distribution of atoms can be measured too. In a momentum distribution, there is a clear difference between a superfluid state and a Mott insulator state. In a superfluid state, atoms in different lattice sites will maintain a fixed phase difference and this means that atoms will interfere with each other coherently to produce a matter wave interference pattern. On the other hand, in a Mott insulator state, atoms are localized in each lattice site and the number of atoms in each lattice site is fixed. This means that there is no coherence between atoms in different lattice sites and there will be no interference between them.

The first experimental demonstration of a quantum phase transition with ultracold atoms in an optical lattice was done by M. Greiner et al. [29]. They showed the disappearance of interference peaks with the increase of the optical lattice depth and the existence of a gap to the excitations.

4.2 Experimental set up

4.2.1 Three dimensional optical lattice

For this experiment the new BEC set up described in Ch. 2 was used. Ultracold atoms were prepared from a BEC with up to 2 million atoms. A 3-D optical lattice was made of three orthogonal standing waves. Fig. 4.1 shows the configuration of optical lattice beams. One beam is along the axial direction of the magnetic trap and two beams are in the radial directions. Both radial beams have 45 degree angle relative to horizontal and vertical axis.

Intensity of these three standing waves can be written (we used orthogonal polarizations for three beams) $I(x, y, z) = I_0(\sin^2(kx)+\sin^2(ky)+\sin^2(kz))$. The amount of ac stark shift and scattering rate can be calculated easily in the limit of large detuningg.

$$V = -\frac{\hbar\Omega^2}{4\Delta} \tag{4.5}$$

(where V is the ac stark shift from lattice laser beams, Ω is the Rabi frequency of lattice laser beams, and Δ is the detuning of laser beams from the atomic resonance.)

For ^{87}Rb D2(780 nm) and D1 (795 nm) transitions need to be included for the estimation of the optical lattice depth.

$$V(x, y, z) = -(\frac{\hbar{\Omega_1}^2}{4\Delta_1} + \frac{\hbar{\Omega_2}^2}{4\Delta_2}) \tag{4.6}$$

(where we added the ac stark shift from each transition.)

Scattering rate can be also can be written in the limit of a large detuning.

$$\gamma_{\mathrm{sc}}(x, y, z) = \frac{\hbar^2{\Omega_1}^2}{4\Delta_1^2}\Gamma_1 + \frac{\hbar^2{\Omega_2}^2}{4\Delta_2^2}\Gamma_2 \tag{4.7}$$

(where Γ is the decay rate of the excited state.)

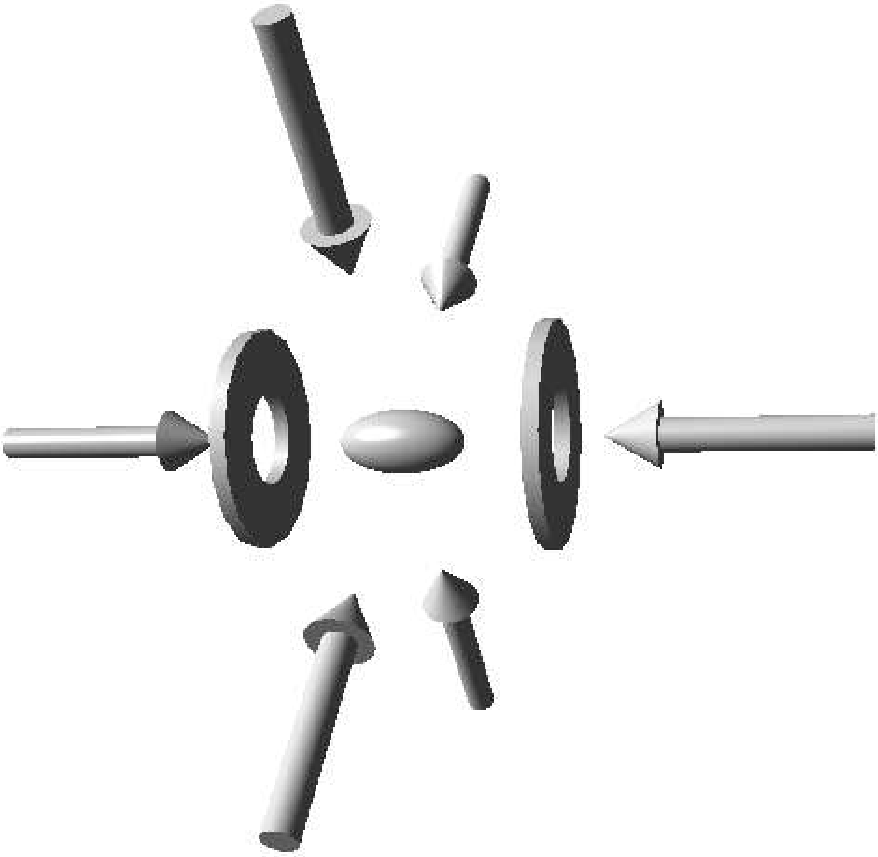

Figure 4.1: 3-D optical lattice set up. Two magnetic coils are shown and two radial direction optical lattice beams are 45 degree to vertical and horizontal directions. Imaging direction is horizontal or vertical which will be 45 degree to radial direction optical lattice beams

There is a restoring force for atoms to be trapped at the highest intensity region for the red detuned laser beams from ac Stark shift of ground state atoms. With this effect, atoms will be trapped in individual lattice sites and these three orthogonal standing waves will form a 3-D optical lattice for atoms. Accurate calculation of trap depth and photon scattering rate can be done with the given formula.

A Ti-Sapphire laser (Coherent model 899-01) was used to produce the optical lattice laser beams. This laser was converted to a single frequency laser with the addition of ICA (Intra Cavity Assembly). The laser beam coming out of 899-01 laser goes through a 30 MHz AOM to control the optical lattice laser intensity. Then 1st order beam was sent to the experimental optical table via an optical fiber. In the experimental optical table, main optical lattice beam goes thorough two AOM's to produce three laser beams with different frequencies and also to control the power of each beam. Different frequencies are necessary to avoid interference among different lattice beams in case the polarizations are not exactly orthogonal. These three beams were delivered to the BEC chamber through optical fibers to improve the beam quality and alignment stability. Finally, each incoming beam from optical fibers was retro-reflected to form three standing waves. We set the waist of standing waves to be 260 micron for the radial beams and 130 micron for the axial beam. The windows are made of optical quality fused silica disc which make it possible to have a very small distortion of the lattice beams.

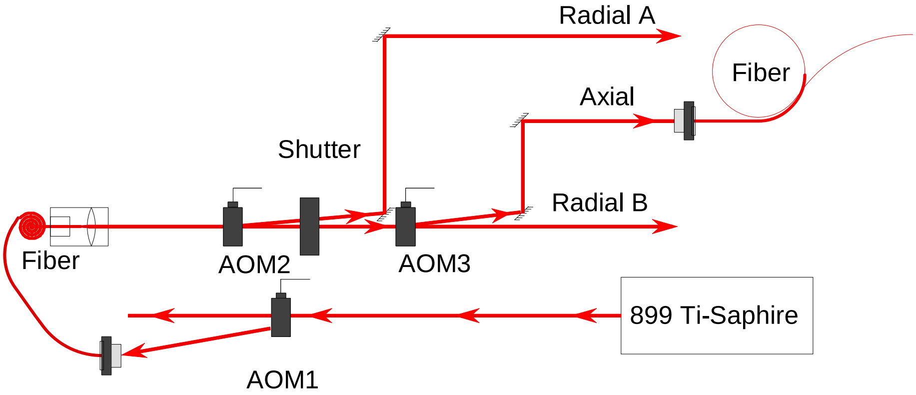

Figure 4.2: Optical lattice beam set up. AOM1 has a frequency of 30 MHz, AOM2 has a frequency of 250 MHz, and AOM3 has a frequency of 50 MHz.

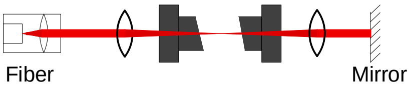

Figure 4.3: Optics set up for the individual lattice beams for the experiment. The location of fiber output coupler, the lens, the retro-reflecting mirror, and the focal length of the lens was chosen to have a chosen waist at the center of the chamber.

4.2.2 Optical lattice alignment and calibration

To align all three beams on to the center of the BEC is not an easy task and it requires a series of steps. The wavelength of the Ti-sapphire laser can be tuned over a wide range (770nm-900nm) and because optical fibers were used for the final delivery of the optical lattice beams, alignment after the optical fiber was not affected by any change of the wavelength.

First, we tuned the wavelength of the optical lattice laser to ^{87}Rb D1 or D2 resonance and blocked the retro-reflected beams to align incoming beams first. With resonant light, we align each incoming beam onto the dark MOT cloud by looking at the loss of atoms from the dark MOT. We used XY translational stages which translate the lenses focusing lattice beams on the BEC to move optical lattice beams. After three incoming beams were aligned onto the dark MOT, we started to use a BEC as our alignment target. After making a BEC, a short pulse of lattice laser beams was applied to a BEC. There was a decrease of the number of atoms in a BEC due to the scattering loss. Lattice laser beams could be aligned by maximizing the loss. After this step, we detuned 899-01 to a longer wavelength typically 1 - 2 nm away from the resonance and at this wavelength, the optical lattice laser beams have a very strong dipole trapping effect without too much scattering loss. After ramping up the optical lattice laser beams power atoms in a BEC can be trapped in an optical trap. The optical trap formed by the lattice beams is stronger than magnetic trap. Therefore if there is any misalignment between magnetic trap center and optical lattice beam center, there will be a displacement of the BEC position from the BEC position without the optical lattice. Two orthogonal imaging directions were used for the accurate alignment of all three beams. With this technique, we can match the center of lattice beams to the center of a BEC. We usually tried to align them until we saw no displacement of the BEC position within our resolution limit (6 μm).

To align retro-reflected beams, we used the fact that we were using optical fibers for the final delivery of laser beams to the chamber. If the retro-reflected beam is aligned, this beam will also be coupled back into the optical fiber. Retro-reflection alignment was done by maximizing the power coupled back into the optical fiber. We typically checked the final alignment by observing the position change due to the each optical lattice beam with the retro-reflected beam. Once we aligned them, the alignment turned out to be quite stable up to a few weeks.

Although the optical lattice depth can be calculated easily with the knowledge of beam waist, detuning, and beam power, it is important to check the calibration of the optical lattice depth independently considering the uncertainty we have in measuring the important parameters. For the purpose of the calibration, a diffraction of atomic wave packet with a very short standing wave was used [50] [51]. After turning off the magnetic trap, a very short optical lattice beam pulse was sent to the BEC. The duration of this pulse should be much shorter than the period of atomic motion in a ground state of a single lattice site. With this condition, the effect of the optical lattice pulse can be thought of imprinting phase variation on an atomic packet wave function.

$$\Psi = \Psi_0 e^{-i\alpha cos(2kx)} \tag{4.8}$$

($\alpha = \frac{V_0\tau}{2\hbar}$ and V_0 is the optical lattice depth and τ is the pulse duration.)

This wave function can be expanded with different momentum components and the ratio between different momentum components can be calculated easily. By measuring the ratio of atoms in different momentum orders, the optical lattice depth can be estimated. The relation between the number of atoms in the central peak and the first order peak is $\frac{J_0^2(\alpha)}{J_1^2(\alpha)}$. With this method, the optical lattice depth for all three directions were calibrated. The optical lattice depth we found was within 20 % of the value we expected from the waist size and power of the lattice laser beam.

With the condition of our 3-D optical lattice, we can get 70 E_R optical lattice depth for all three directions at 810 nm and 30 E_R at 830 nm.

4.2.3 Loading atoms into the optical lattice

Before loading atoms in a BEC into the optical lattice, magnetic trap strength was typically relaxed down to 20.7 Hz (radial) and 11.6 Hz (axial) to reduce the initial density of atoms. It is necessary to reduce the density of atoms because due to the tight confinement of optical lattices, the three body loss rate will be very high if there are more than three atoms in a single lattice site. Because of gravitational sag, by changing the radial trapping frequency, we are actually changing the vertical position of the BEC. For our trap condition, the amount of displacement is 1.2 mm. To minimize the residual oscillations after the ramping down of the trap strength, we changed trap strength slowly (500 ms duration).

We need to be careful not to excite the atoms from the ground state when we load them on to a 3-D optical lattice because a quantum phase transition can be achieved only when the system remains in the many body ground state. We tried to optimize the ramping up process to minimize excitations. After ramping up and ramping down the optical lattice, the final BEC fraction was measured and with this as a criterion, ramping process was optimized to give the maximum BEC fraction. A quadratic increase and decrease of optical lattice depth with 50ms ramping time was the optimum process for our condition. Intensity of optical lattice beams should be very stable to minimize any excitations. The power of a main optical lattice beam after the first optical fiber was monitored with a photodiode and the power was controlled with a feedback to the RF power going into the main lattice AOM.

4.3 Quantum phase transition from a superfluid to a Mott insulator

A TOF absorption imaging was used to study the quantum phase transition from a superfluid to a Mott insulator. After ramping up the optical lattice depth to the final depth, the optical lattice and the magnetic trap were turned off suddenly and after 20 ms TOF, the density distribution of atoms which reflected the momentum distribution at t=0 was measured.

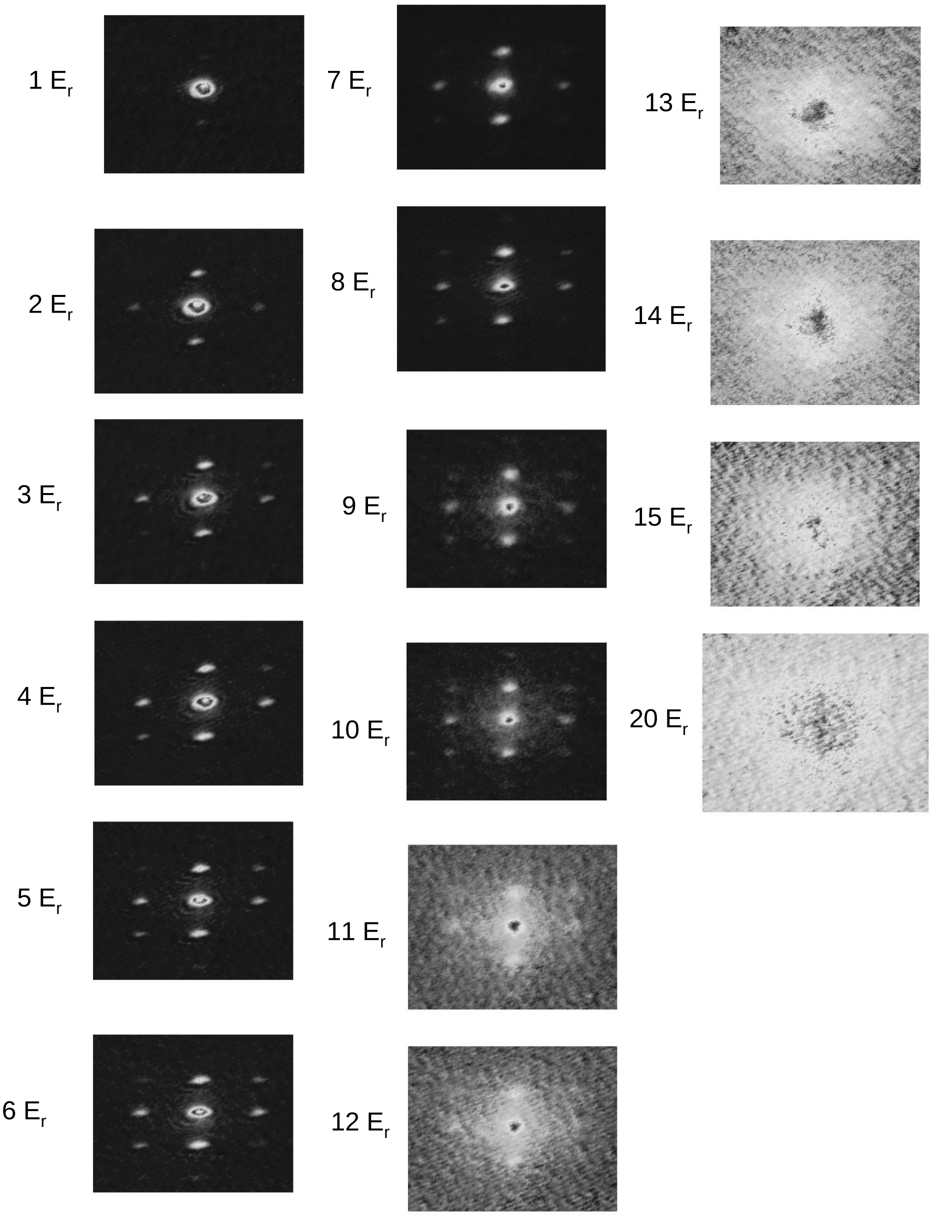

Figure 4.4: Matter wave interference peaks after 20ms TOF. After ramping the 3-D optical lattice depth up to the final depth, the magnetic trap and optical lattice beams were turned off suddenly.

Fig. 4.4 shows the typical examples of matter wave interference patterns. With the increase of the optical lattice depth, side peaks in addition to central peak began to emerge and the difference in distance between central peak and side peak in radial and axial directions was due to the imaging direction which is between two radial direction lattice beams.

The interference peaks fade away with the increase of the optical lattice depth. We tried to study this change more quantitatively by looking at the radial and axial cross sections. These cross-sections were fitted with the sum of four gaussian distributions. Fig. 4.5 shows the cross sections and fittings.

By looking at these cross sections carefully, two different trends in our data are obvious. First, there is a gradual increase of the broad gaussian distribution with the increase of the final optical lattice depth but the widths of interference peaks remain almost same. Past a specific optical lattice depth, suddenly, there is an increase in the widths of interference peaks and eventually there is no interference peak left at very high optical lattice depths.

We think that the increase of the broad peak is mainly due to the depletion of the BEC fraction with the increase of effective interaction between atoms coming from the tight confinement. Measured ratio of atoms in coherent peaks and incoherent background is plotted in Fig. 4.6. There is no sudden change in this ratio with the increase of the optical lattice depth. The right indication of the transition might be the sudden increase of the width of the central peak which was pointed out by Zweger et. al. [53] and also preliminary experimental study of this effect was done by T. Esslinger et. al. [52]. The

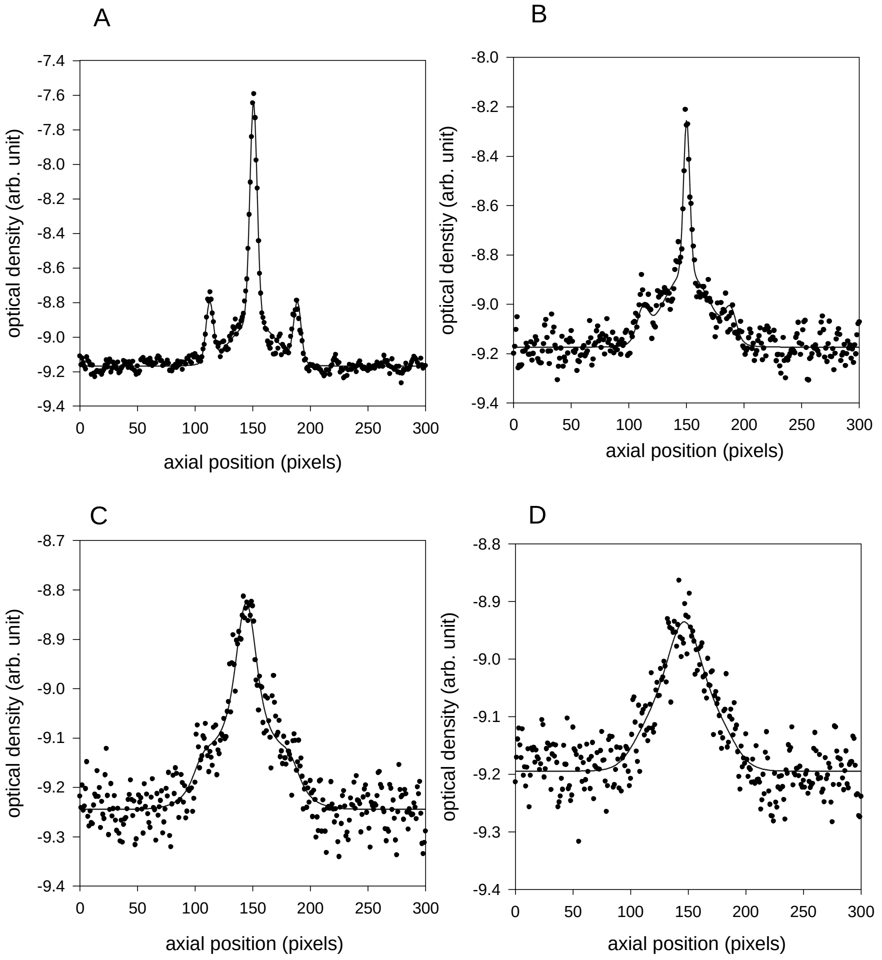

Figure 4.5: Cross-section and fitting of an interference peak image. One pixel is 6 μm. A. 10 recoil energy (U/zJ=2.1) B. 12 recoil energy (U/zJ=3.9) C. 13 recoil energy (U/zJ=5.3) D. 16 recoil energy (U/zJ=11.9).

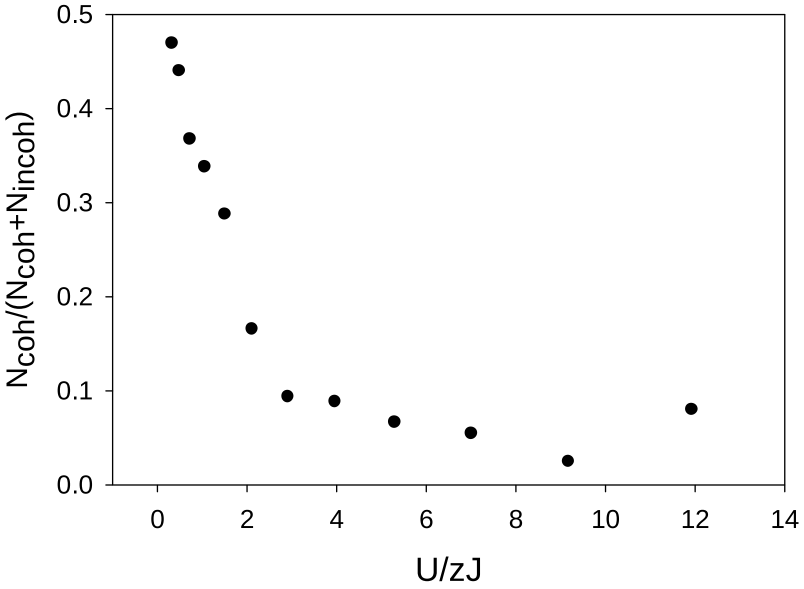

Figure 4.6: Ratio of coherent and incoherent atoms

width change as a function of the optical lattice depth was plotted and the clear increase of the width of the central peak can be seen when the optical lattice depth crosses the critical value.

To verify that our system remains close to the many body ground state, the following test was done. The optical lattice was ramped up to 20 recoil energy and held them for 30 ms and ramped down to 6 recoil energy and took a TOF absorption image. We found that we could recover the interference peaks which shows that our system is close to the many body ground state all the time.

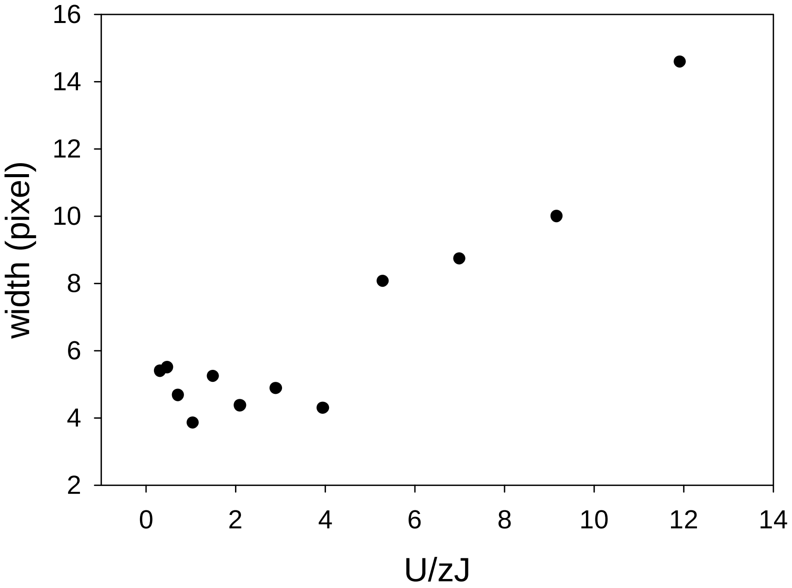

Figure 4.7: Width change of the central peak. Vertical axis is in a unit of one pixel which is 6 μ m.

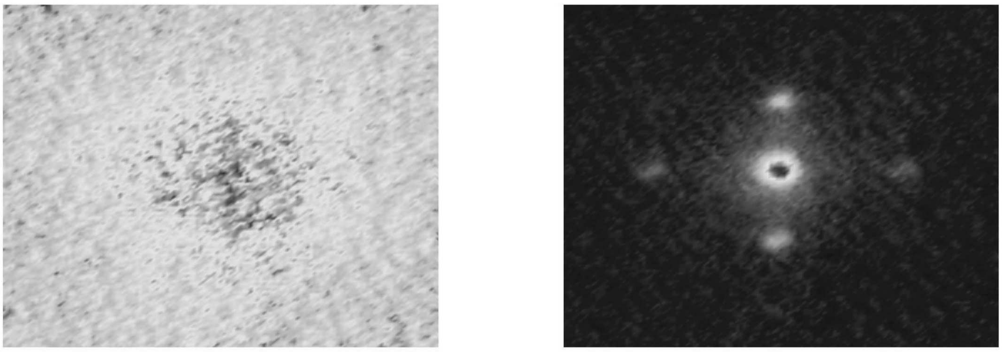

Figure 4.8: Reappearance of an interference peak. The left picture is taken after ramping up the optical lattice to the 20 recoil energy. The right one is taken with the process of ramping up the optical lattice to 20 recoil energy, hold atoms in an optical lattice for 30ms, and ramping down the optical lattice depth to 6 recoil energy.

Chapter 5

Raman photoassociation of a Mott insulator

As described in Ch.2, ultracold molecules produced from ultracold atoms via photoassociation suffer from inelastic collisions between atoms and molecules. This will be the ultimate limitation in converting ultracold atoms into ultracold molecules unless molecules are prepared in a ro-vibrational ground state. However there have been rapid developements in creating ultracold bosonic molecules from ultracold fermionic atoms [56]. Due to the fermionic nature of atoms and a very small binding energy which means the big size of molecules, the inelastic collision rate between atoms and molecules for fermionic atoms is very small [54]. In fact several groups produced a molecular BEC with ultracold molecules from fermionic atoms [55]. But ultacold molecules formed by bosonic atoms do not have this property and will decay very fast with atom-molecule collisions.

Ultracold atoms in an optical lattice is a great system to study a quantum phase transition and other phenomena of strongly interacting system. Also it turns out that this system is a good starting point for the efficient molecule formation. As explained in the previous chapter, ultracold atoms in an optical lattice have an external trapping potential and can have several different Mott domains. And atoms trapped in an each lattice site are isolated from atoms in other lattice sites and this isolation and a Mott domain with two atoms per site will be a perfect combination for the efficient molecule production. Ultracold molecules in an optical lattice produced from ultracold atoms in an optical lattice will be a very interesting system to study. Already there is a very interesting theoretical proposal to do a quantum computation with polar molecules trapped in an optical lattice [30] and because of a large enhancement factor, utracold polar molecules trapped in an optical lattice will be a perfect choice for an electron EDM search [11].

5.1 Photoassociation of a Mott insulator

5.1.1 Creation of molecular quantum gas in an optical lattice

D. Jaksch et. al. [57] first proposed to create ultracold molecules from a Mott insulator with two atoms per site. By definition a Mott insulator does not have any number fluctuation within its domain and due to the high optical lattice depth, tunnelling between different lattice sites will be greatly suppressed. These are ideal conditions to produce molecules without worrying about the collisions between atoms and molecules. If molecules are produced coherently, molecules will remain in the many body ground state. There is an interesting possibility of creating a molecular BEC by ramping down the optical lattice after the creation of molecules in an optical lattice. Also depending on the molecule-molecule scattering length, molecules might be in a Mott insulator state. These ultracold molecules in the optical lattice can be a very

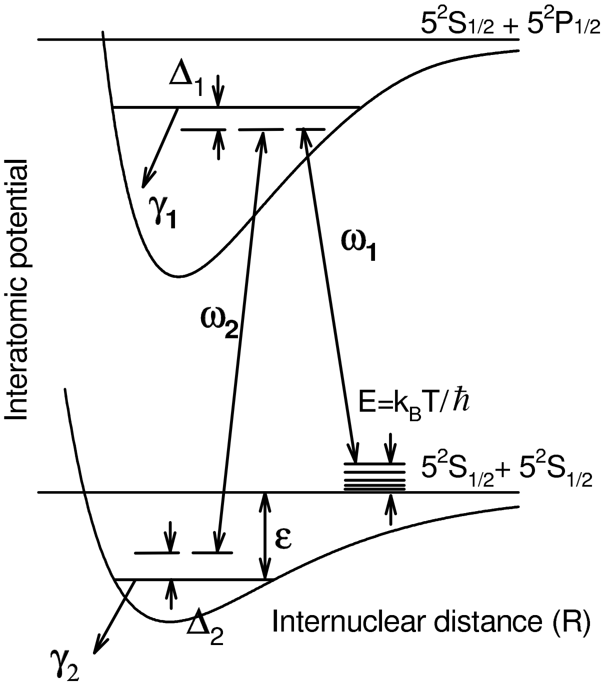

Figure 5.1: Two color Raman photoassociation schematic

good starting point to make real ground vibrational state molecules which are stable against collisions. This shows the possibility of new experiments with ultracold molecules in an optical lattice.

As discussed in Ch.2, Feschbach resonance or photoassociation can be used to convert two atoms into a molecule. We chose to use photoassociation to produce ultracold molecules. Single color photoassociation which was used in the experiment described in the Ch.2 can produce triplet ground state molecules via spontaneous decay but this process is incoherent and there can be several different final states populated. To overcome this problem, Raman photoassociation has been used to produce molecules with the selected ro-

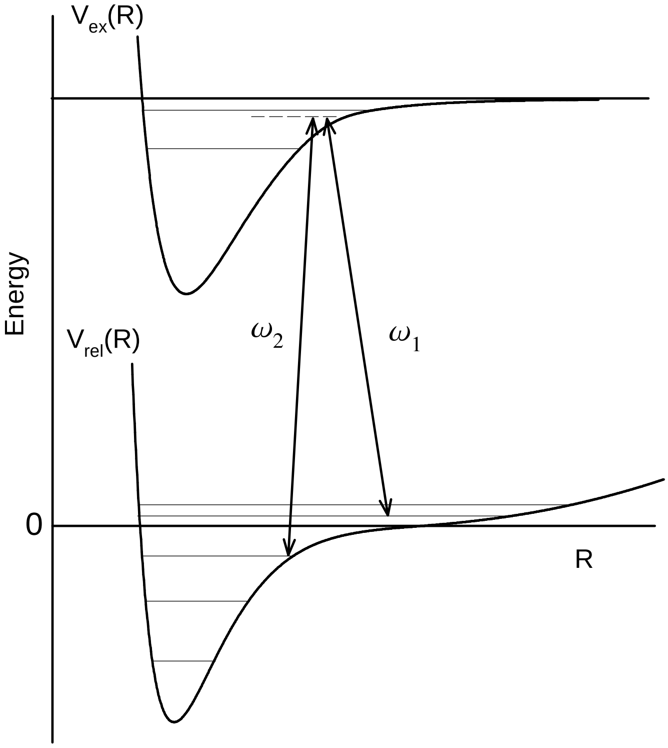

Figure 5.2: Two color Raman photoassociation with atoms in an optical lattice. Trapping potential in a longer range was exaggerated to show the difference in potential curve from optical lattices potential.

vibrational state. Raman photoassociation uses two laser beams whose energy difference will be same as the binding energy of the intended ground state molecules [41]. Fig. 5.1 shows the typical Raman photoassociation process. Two free atoms can absorb a photon from the laser 1 with frequency ω_1 and undergo stimulated emission by the laser 2 with frequency ω_2 to make a triplet ground state molecule. Intermediate detuning to the excited molecular state needs to be chosen carefully to optimize the Raman photoassociation rate over an off-resonant Raman scattering rate. If a Raman photoassociation pulse was applied to two atoms per site Mott insulator, there will be a resonant coupling between two free atoms and a molecule. This will be very close to a textbook example of two states coupled to each other but in this case between two different chemical species. There will be Rabi oscillations between atoms and molecules with this resonant coupling. If an exact π pulse was applied, all the atom pairs in a Mott insulator will be converted into molecules.

The strong trapping potential from optical lattices will affect the nature of Raman photoassociation coupling. Fig. 5.2 shows the schematic of Raman PA with atoms in optical lattices. First of all, typical trapping frequency of 30 kHz makes it possible for atoms to have a discrete energy level in optical lattices. With the seperation between the center of mass and relative coordinates of two atoms, it will be easy to see that both center of mass motion and relative motion have zero point energy which will affect the Raman transition frequency. This point will be important in a latter section. Also due to this tight confinement, the Raman PA transition strength will be enhanced.

To make this scheme work, first we need to prepare two atoms per site Mott insulator. Due to the magnetic trap, we have an inhomogeneous density distribution which causes the formation of several different Mott domains. The theoretical simulations of what this distribution will be have been performed by several groups but there is no 3-D optical lattice simulation with our experimental conditions. There is a mean field theory to describe the change of overall shape of an atomic cloud in an optical lattice [58]. Although mean field theory cannot be applied to our experiment which needs quantum simulations to get a correct answer, we can get some qualitative idea of the atomic cloud shape change during the ramp up of the optical lattice. This theory tries to get a macroscopic density distribution averaged over one lattice cycle. The usual Thomas-Fermi distribution can be applied to describe this density distribution with the only change of an atom-atom interaction parameter. The increase of this interaction parameter is due to the increased confinement from the optical lattice potential and it can be calculated.

$$g = \frac{4\pi\hbar^2 a}{m} \tag{5.1}$$

$$g' = g(d \int f_0^4(x))^3 \tag{5.2}$$

($f_0(x)$ is the Wannier function for the optical lattice potential and d is the spacing between adjacent lattice sites.)

We can do a simple estimation by assuming that $f_0(x)$ is just the wave function of the ground state of a harmonic potential which will be a very good approximation of the single lattice well potential. There will a quantum phase transition from a superfluid ot a Mott insulator around the optical lattice depth of 13 recoil energy. The density distribution afterwards will be outside of mean field theory and knowing the density distribution at the transition point will help us to understand the condition needed to achieve two atoms per site Mott insulator. At $\mathrm{V}_0 = 13$, $g' = 13.5g$ and Thomas-Fermi radius will be also increased.

$$R_{TF} \propto \frac{g^{1/5}}{\omega^{2/5}}$$

Due to the dipole trapping effect coming from the inhomogeneous intensity distribution of optical lattice laser beams in the transverse direction, there will be a change of trapping frequencies. With the beam size and lattice beam geometry we used, there will be a substantial increase of the trapping frequencies. The magnetic trapping frequencies without optical lattices are $\nu_z = 11.6$ Hz, $\nu_r = 20.7$ Hz. With optical lattices of 13 recoil energy, the trapping frequencies become $\nu'_z = 27.0$ Hz, $\nu'_r = 43.5$ Hz. Thomas-Fermi radius will change too.$R'_z = 1.23R$ $R'_r = 1.2R$

With this change of the radius of Thomas-Fermi radius, the peak density of atomic cloud changes too. $n'_0 = 0.55n_0$

To estimate the number of atoms per site distribution, we can assume that if the density of atoms is in the range of $N - 0.5 < n < N + 0.5$ (with unit of number of atoms per site) number of atoms at that point will be N after the transition into a deep Mott insulator regime. This will give us a rough estimate of number of atoms per site distribution.

Although this theory gives us some guidance of how many atoms per site will be at the center, it's important to determine this distribution experimentally. We found that Raman photoassociation is a very useful tool to determine the distribution of Mott domains with different number of atoms per site. Due to the difference in on site interaction energy change during Raman photoassociation process between two atoms per site and three atoms per site Mott insulators, there will be a shift in Raman photoassociation resonance frequency. If the shift is big enough, we can selectively photoassociate two atoms per site Mott insulator or three atoms per site Mott insulator by choosing an appropriate Raman frequency. With this method, the relative population between two atoms per site Mott insulator and three atoms per site Mott insulator can be determined.

5.1.2 Raman photoassociation resonance frequency with utlracold atoms in an optical lattice

In our previous experiment, ultracold molecules were produced from a atomic BEC and this production was observed by the decrease of the number of atoms when a Raman frequency satisfied the resonance condition. Careful measurement of the line shape of the Raman frequency scan was done and by measuring the shift of the Raman resonance frequency as a function of the density of atoms, an atom-molecule elastic scattering length was estimated [41]. As shown in that work, careful understanding of the Raman resonance frequency is important and there are a few differences between Raman photoassociation of an atomic BEC and Raman photoassociation of a Mott insulator. The biggest difference comes from the fact that atoms are localized in a very tight trap in a Mott insulator state and trapping frequency is up to 30 kHz which is much bigger than the typical trapping frequency of a magnetic trap which is about 100 Hz. Two free atoms will have quantized energies in a single optical lattice site and Raman resonance frequency will be shifted due to the zero point energy in a harmonic potential. The next difference is due to the mean field energy change. In a BEC, we will have a mean field energy change from two atoms in an atomic BEC and one molecule in an atomic BEC. But for two atoms in a single lattice site, there is on-site interaction energy before Raman photoassociation but after Raman photoassociation, there will be no on-site interaction energy because there is only one molecule in a single lattice site.

$$\hbar\Delta\omega_{Raman} = \mathrm{E}_{binding} + \frac{3}{2}\hbar\omega_0 + \Delta E_{acStark1} + \Delta E_{acStark2} + U_{a-a} \tag{5.3}$$

Above equation describes the Raman resonance frequency for two atoms per site. $\mathrm{E}_{binding}$ is a binding energy of a molecular state, ω_0 is the harmonic trapping frequency of a single optical lattice site, and U_{a-a} is the on site interaction energy between two atoms. There will be an ac Stark shift of molecular binding energy and two free atomic state energy from Raman photoassociation laser beams ($\Delta E_{acStark1}$) and optical lattice beams ($\Delta E_{acStark2}$). These ac Stark Shifts are proportional to the power of the laser beams and can be measured very easily by monitoring the Raman resonance frequency change as a function of the laser beam power. Because of close detuning to Rb D1 line, Raman photoassociation laser beams have a relatively big ac Stark shift compared to the optical lattice laser which has 20 - 40 nm detuning. In our experiment, $v = 39$ state in triplet ground state was used for the molecular state and this state has a binding energy of 636.0094 MHz. The harmonic trapping frequency ω_0 at the optical lattice depth of 20 recoil energy is 29.8 kHz. U_{a-a} at the same condition is 1.9 kHz. The biggest shift comes from ac Stark shift of Raman laser beams and with the typical condition we used (60 mW total power and 3.9 GHz detuning from the intermediate state), there was 96 kHz frequency shift. For optical lattice laser beams, we actually tried to use a frequency at which there is no ac Stark shift and this was done experimentally by measuring the ac Stark shift as we vary the frequency of the optical lattice laser. All of this suggests that to observe the Raman resonance frequency, we need to be very careful in stabilizing frequencies and intensities of the laser beams.

Same calculation can be done for three atoms per site and the only difference will be on-site interaction energy change. Fig. 5.3 shows the schematic of this difference in the on site interaction energy.

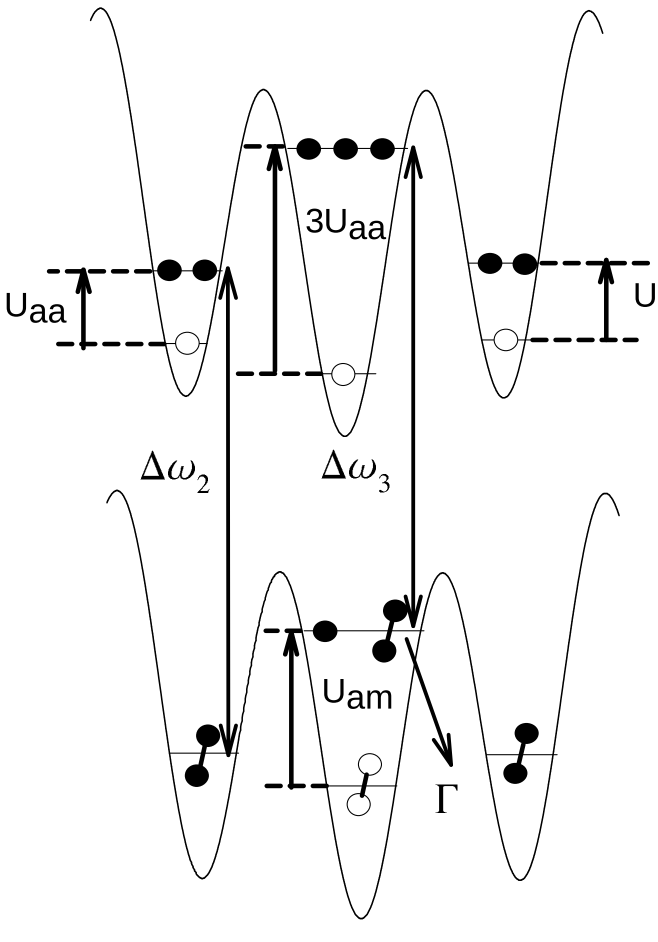

Figure 5.3: Raman frequency shift between N=2 and N=3 Mott insulators

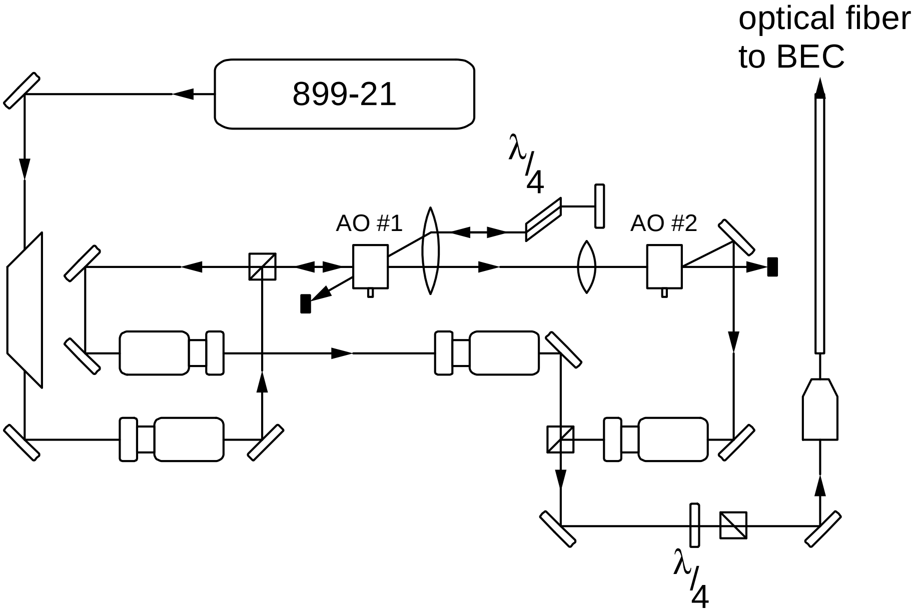

Figure 5.4: Raman photoassociation laser beams set up

$$\hbar(\Delta\omega_{3,Raman} - \Delta\omega_{2,Raman}) = 2U_{a-a} - U_{a-m}$$

Experimental effort to measure this shift will be reported in later sections.

5.2 Experimental set up

5.2.1 Raman photoassociation laser set-up

The same 3-D optical lattice set up described in the previous chapter was used in this experiment. By ramping up the optical lattice depth, two atoms per site Mott insulator can be prepared for Raman photoassociation. A Ti-Sapphire laser (Coherent model : 899-21) was used for the Raman photoassociation. For Raman photoassociation, we need to have two laser beams with fixed Raman frequency difference and need to be able to chage the detuning from the intermediate level. We followed the same kind of optics and AOM arrangement which was used in the previous experiment done with the old BEC set up [38].

Fig. 5.4 shows how we split the laser beam into two Raman beams with tunable Raman frequency. As explained in Ch. 2, 899-21 laser was frequency stabilized by locking it to the optical cavity whose length was stabilized by locking it to the stable MBR laser which was locked to the atomic absorption cell. This locking set up makes it possible to lock the 899-21 laser to the frequency chosen with a stability of 1 MHz over a few hours. As shown in figure, two beams were combined into a single optical fiber which makes it possible to have an identical alignment for two Raman beams. We also need to align Raman beams onto the BEC and we used the same method we used for the optical lattice beam alignment.

We need to choose the excited state we are going to use and intermediate detuning for Raman photoassociation of a Mott insulator. Careful study of the ratio between coherent coupling rate over inelastic loss rate was done by Roahn Wynar [38]. Although this calculation was for Raman photoassociaion of a BEC, the relative merit between different excited states will remain same. Based on his thesis we chose a molecular excited state bounded by -28 cm^{-1} in $0_g^{-1}(\mathrm{P}_{1/2})$ potential for our Raman photoassociation experiment and used several different intermediate detunings from 150 MHz to 12 GHz.

As pointed out in the previous section, we have a large ac Stark shift in our Raman resonance frequency which means that the intensity of Raman beams need to be very stable to maintain same Raman resonance condition. To accomplish this the total power coming out of fiber after the chamber was monitored with a photodiode and stabilized with feedback to the AOM for the first Raman photoassociation beam.

$$\Delta \mathrm{E}_{acStark} \propto \frac{I_1}{\Delta + 0.636} + \frac{I_2}{\Delta} \tag{5.4}$$

This equation shows the ac Stark shift from the first Raman laser and the second Raman laser. Usually $\Delta = 3.9\mathrm{GHz}$ was used and $I_1 = 3I_2$. With this condition, ac Stark shift from the first and second Raman laser were very similar at the same intensity. We tried to maintain the same ac Stark shift with the fixed total intensity. ac Stark shift fluctuations due to the fact that we only controlled the first Raman photoassociation laser intensity was very small. If there was 10 % fluctuation of total power, there can be only about 0.4 % variation of ac Stark shift.

5.2.2 Experimental procedure

A Raman photoassociation experiment is a relatively complicated experiment and needs a very careful planning. Firstly, a good BEC production needs to be shown and optical lattice laser beams and photoassociation laser beams power and alignment should be checked based on the method described in the previous chapter. At this point frequency locking of Raman photoassociation laser should be enabled and intensity locking of optical lattice laser and Raman photoassociation laser should be maintained. With all the lasers working fine, we're ready to do the Raman photoassociation experiment. One important condition to achieve a good data of a Raman photoassociation experiment is the stability of the BEC production. Because destructive imaging was used in our experiment, the number of atoms in the BEC should not vary too much and it was possible to obtain a number stability of 10 % fluctuation. As discussed before, this stability was possible with a new servo control of the cooling water temperature. Also it took 30-40 cycles before we got into a stable working condition. After we got a stable BEC production and all beams were aligned, first Raman photoassociation scan was done without an optical lattice. Typically 50-100 ms photoassociation pulse duration was used and Raman resonance frequency could be found very easily with up to 60 - 70 % loss of atoms. And then we checked the ac Stark shift of the optical lattice laser. With retro-reflections blocked, optical lattice beams became a simple dipole trap for atoms and by measuring the shift of Raman resonance frequency, ac Stark shift could be determined. Typically, we wanted to have no ac Stark shift from optical lattice laser by tuning frequency of optical lattice laser until there was no ac Stark shift.

After this preparation, two atoms per site Mott insulator could be produced by ramping up a 3-D optical lattice up to the final optical lattice depth. With a fixed pulse duration of about 20-40 ms, Raman photoassociation scan was done again and there was a frequency shift which was discussed in a previous section. After this step, we could do a real study of a Raman photoassociation of a Mott insulator. The results will be discussed in later sections.

5.3 Raman photoassociation of a BEC with new BEC set up

Before we started to do a Raman photoassociation of a Mott insulator, we repeated the Raman photoassociation experiment we did with our old BEC set up. One of the main limitation we had in our previous set up was the existence of oscillations of the BEC cloud which caused the broadening of our Raman photoassociation linewidth. Because of this we could not try to observe coherent oscillations between atoms and molecules. We tried Raman photoassociation with the BEC without optical lattices to check the set up for Raman photoassociation, to see the difference from the previous experiment, and possibly to see the coherent transfer of atoms to molecules.

To minimize the effect of an atom-molecule inelastic collisions we reduced the density of the BEC by reducing trap frequencies down to $\nu_z = 11.6$ Hz and $\nu_r = 20.7$ Hz. After the preparation of a BEC, a Raman photoassociation pulse was applied with a chosen pulse duration and Raman frequency and the magnetic trap was turned off to measure the number of atoms with a TOF absorption imaging. If molecules are produced, there will be a decrease in the number of atoms and the Raman resonance frequency could be found by scanning Raman frequency while monitoring the number of atoms after a

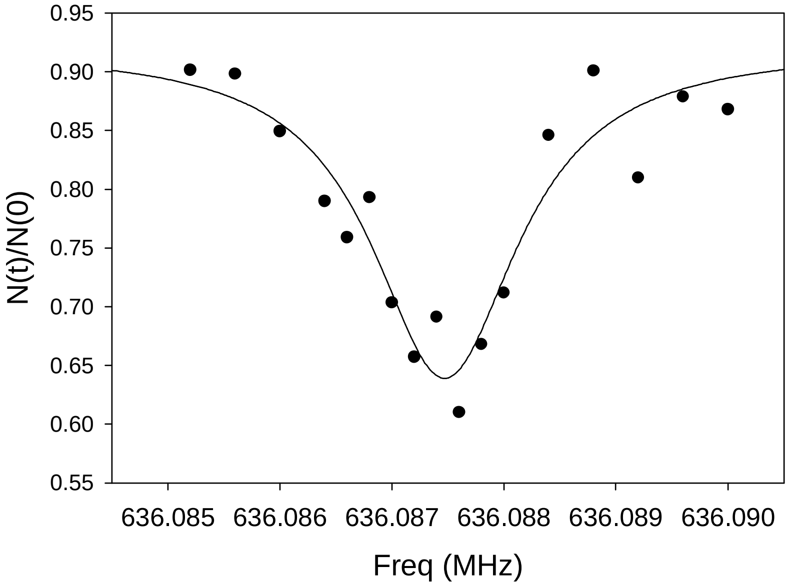

Figure 5.5: PA scan without optical lattice

photoassociation pulse.

We found the clear difference between our result and previous results we got with old BEC set up. Fig. 5.5 shows the Raman PA scan data with new BEC set up. -12 GHz detuning was used and PA pulse duration was 25 ms. From the fitting the width of peak is 1.3 kHz. This width of Raman resonance is much narrower than before which means that coherent coupling rate versus incoherent loss rate is larger than before.

We fixed Raman frequency on resonance and varied Raman PA pulse duration. The results are quite interesting. There is a very small decay for initial few ms and there is a rapid decay and after that, there is a very slow decay. This is not consistent with the picture of inelastic loss dominated

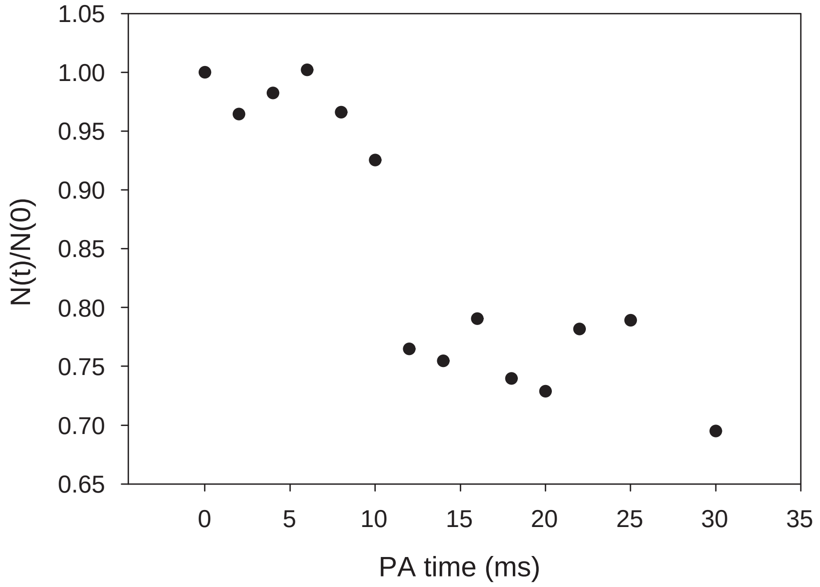

Figure 5.6: PA decay curve without optical lattice

Raman PA process and we tried to understand the origin of this behavior. Further study will be necessary to understand this data.

5.4 Raman photoassociation of a Mott insulator

5.4.1 Single photon photoassociation of a Mott insulator

Before starting Raman photoassciation of a Mott insulator, single photon photoassociation was done to study the possibility of forming multiply occupied sites. To do this experiment, we used very similar experimental sequence we used in Ch.2. A Mott insulator was formed by ramping up the optical lattice to the final optical lattice depth. And then a single PA laser pulse whose energy is resonant between two free atoms and a single excited molecular state was applied to the atoms in a BEC. Eventually, these excited

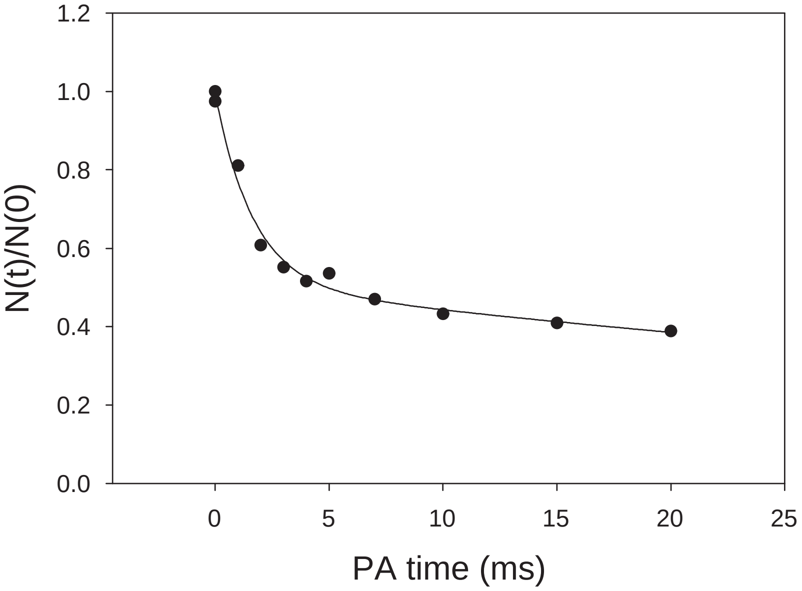

Figure 5.7: Single photon PA decay curve with optical lattice. The fast decay rate is 590 s^{-1} and the slow decay rate is 14 s^{-1}. 49 % of atoms decay fast and 51 % of atoms decay slowly.

state molecules will decay and we can observe the reduction of the number of atoms. We used around 100 mW power of PA laser beam and measured the number of atoms change as a function of PA pulse duration.

The difference between single photon decay curve with an optical lattice and without an optical lattice is very clear. There are two clearly different decay rates in this decay curve. We think that the fast decay component comes from the atoms in multiply occupied sites and the slow decay component comes from the atoms in singly occupied sites. To form molecules, atoms in singly occupied sites need to tunnel into other optical lattice sites and at a very high optical lattice depth, tunnelling rate will be very small. From this data, it is

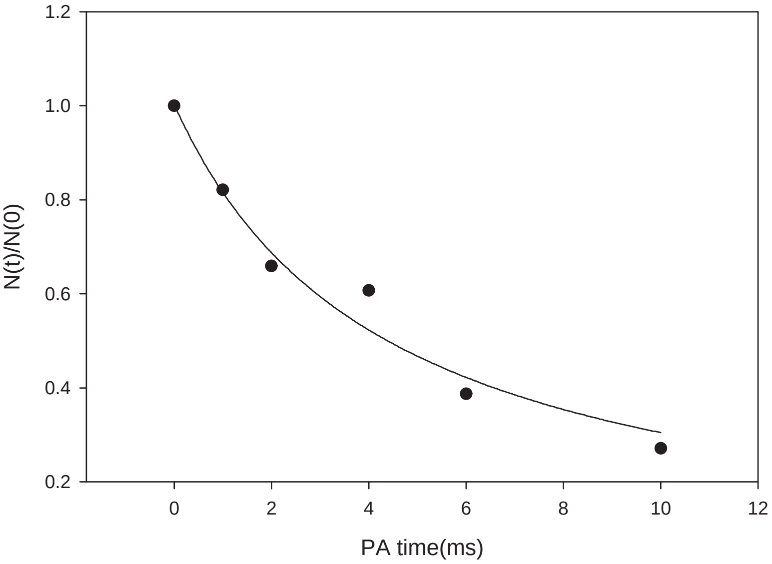

Figure 5.8: Single photon PA decay curve without optical lattice. The decay rate is 138 s^{-1}

evident there are multiply occupied sites in an optical lattice.

5.4.2 Raman frequency shift between two atoms per site and three atoms per site

To do Raman photoassociation, the optical lattice depth was ramped up to the 20 recoil energy and Raman photoassociation beams with chosen pulse duration and Raman frequency difference was applied to the Mott insulator. To measure the number of atoms, we ramped down the optical lattice and used a standard TOF optical absorption image method to measure the number of atoms. Typical power of PA laser is 80 mW for the first PA beam and 20 mW for the second PA beam.

For stimulated Raman photoassociation to work, the frequency differ-

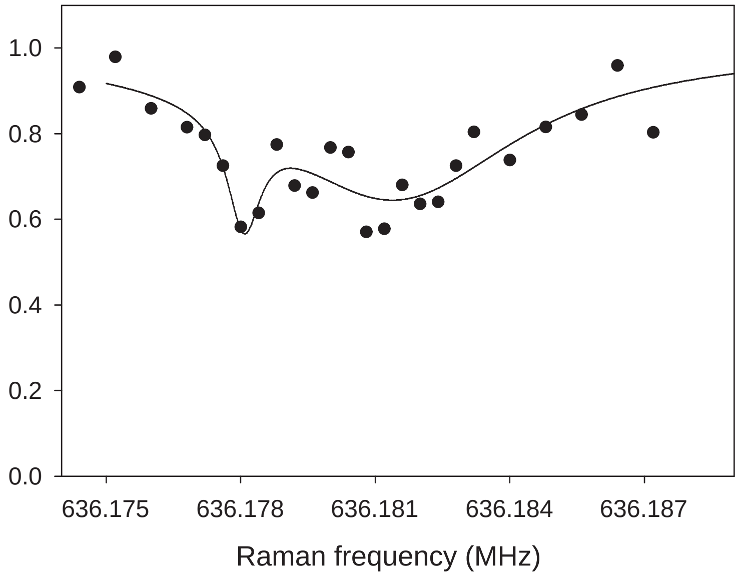

Figure 5.9: Raman frequency scan with 1.6 million atoms

ence between two laser beams should be on resonance condition for Raman transition. To find out this Raman resonance frequency, we monitored the atom number variation as a function a Raman frequency with a fixed pulse duration.

These data sets show the Raman scan data with two different initial number of atoms. There is a clear decrease of the number of atoms from the molecule production when Raman frequency satisfied the resonance condition. But there is a little complicated structure not a single peak. Also peak shape is different between two different initial number of atoms data sets. Especially, the increase of narrow peak in smaller number of atoms data is quite obvious. We tried to understand this structure of the scan. We found that this two peak structure is coming from the population of Mott domains with different

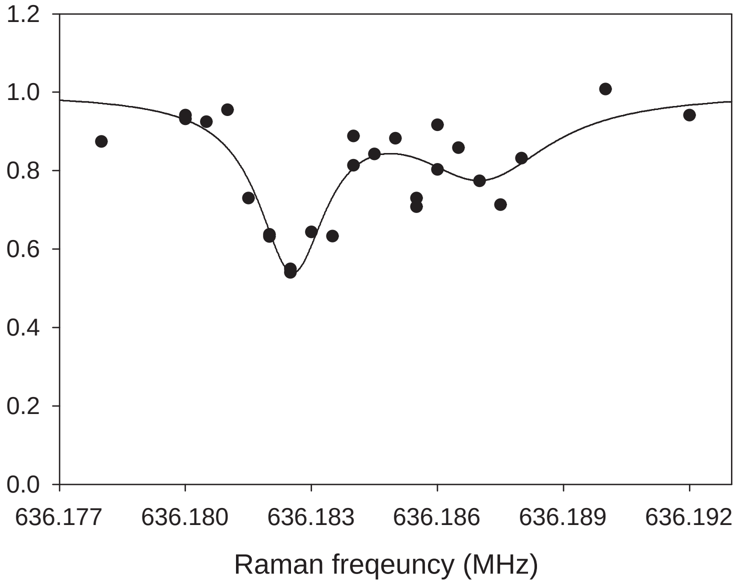

Figure 5.10: Raman frequency scan with 0.6 million atoms

number of atoms per site. It turned out that we can understand the change of this frequency shift as the change of on-site interaction energy between two atoms per site Mott insulator and three atoms per site Mott insulator.

This means that with the measurement of Raman frequency shift between N=2 and N=3 Mott insulators the atom-molecule elastic scattering length can be determined. Also by measuring the width of the Raman peak of three atoms per site, we can actually measure the atom-molecule inelastic scattering rate. In other words, we can determine important interaction parameters between atoms and molecules with single Raman frequency scan data. This will be a very powerful tool to study atom-molecule interactions. Another important point is the possibility of studying Mott insulator domain distribution with Raman photoassociation scan. By measuring number of atoms lost in each peak, we can determine number of atoms distribution in each Mott insulator domain. This will make it possible to study quantum phase transition with different Mott domains distribution and possibly the difference in transition characteristics depending on the number of atoms per site.

5.4.3 Observation of Rabi oscillations between atoms and molecules in an optical lattice

The most exciting possibility with Raman PA of ultracold atoms in an optical lattice is the possibility of realizing coherent conversion of atoms into molecules. The obvious evidence of coherent conversion will be Rabi oscillations between atoms and molecules. To investigate this possibility we did the following experiment. First the Raman frequency scan was done to find out the Raman resonance frequency for the two atoms per site Mott insulator. With Raman frequency locked on the resonance frequency for two atoms per site Mott insulator Raman PA pulse duration was varied. The change in the number of atoms was measured as a function of Raman PA pulse duration.

These two data sets show the sinusoidal variation of the number of atoms as a function of PA pulse duration. These data sets are fitted with the Rabi oscillation with damping rate.

$$\frac{N(t)}{N(0)} = 1 - A + A \times e^{-\gamma t}(\cos\frac{\Omega'}{2}\,t + \frac{\gamma}{\Omega'}\sin\frac{\Omega'}{2}\,t)^2 \tag{5.5}$$

where Ω is Rabi oscillation frequency, γ is the decay rate, and Ω' is $\sqrt{\Omega^2 - \gamma^2}$.

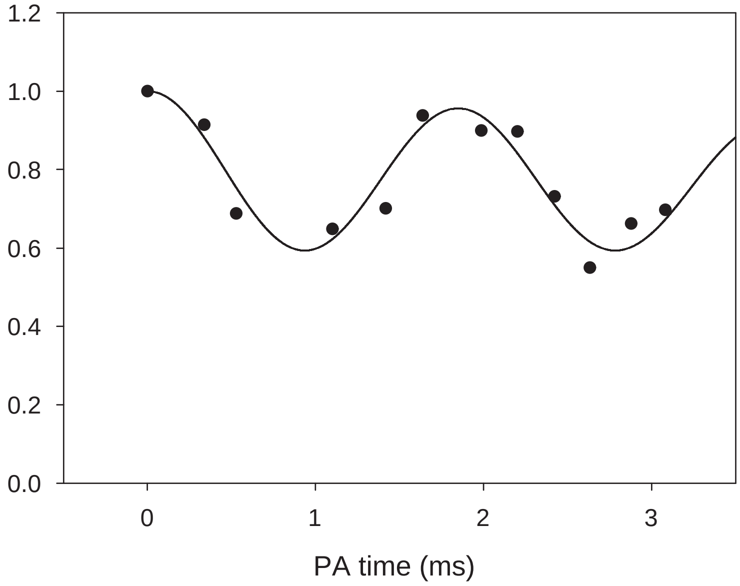

Figure 5.11: Rabi oscillations between atoms and molecules. The number of atoms is 1.9×10^6, the total PA power is 98 mW (the first PA beam power is 68 mW and the second PA beam power is 30 mW.), the detuning is -3.9 GHz, and the optical lattice depth is 15 recoil energy. The data is shown with the fitting where the Rabi frequency is 541 Hz and the damping rate is 9.8 Hz.

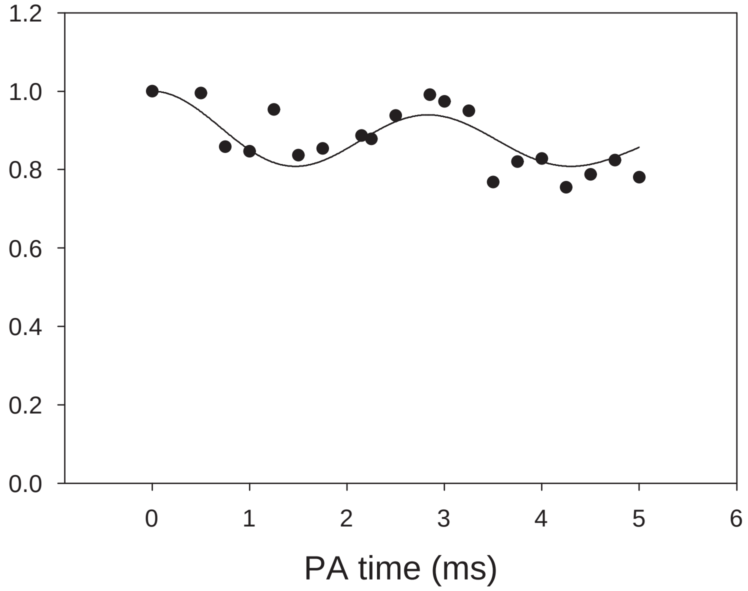

Figure 5.12: Rabi oscillations between atoms and molecules. The number of atoms is 1.7×10^6, the total PA power is 97 mW (the first PA beam power is 73 mW and the second PA beam power is 24 mW.), the detuning is -3.9 GHz, and the optical lattice depth is 20 recoil energy. The data is shown with the fitting where the Rabi frequency is 353 Hz and the damping rate is 21 Hz.

This is the clear evidence of coherent Rabi oscillations between atoms and molecules in an optical lattice. Both data sets shows that the decay rate of molecules produced during Raman PA is around 10-20 Hz which is much smaller than Rabi frequency. This suggests that molecules are creating coherently and this can be seen directly with the reappearance of atoms with the increase of Raman PA pulse. The actual amount of atoms in two atoms per site and the amount of atoms which will be involved in Rabi oscillation can be dependent on many different parameters. And further study is necessary to investigate these issues. But the demonstration of coherent Rabi oscillations between atoms and molecules is the important first step toward the realization of a molecular quantum gas.

Chapter 6

Conclusion

Ultracold Rb_2 molecules were produced via a single photon photoassociation and trapped in a magnetic trap. More than 20 s magnetic trapping was shown without atoms in the trap. There were inelastic collisions between atoms and molecules in the magnetic trap and the inelastic collision rate between atoms and molecules was measured to be $K_{am} = 3.45(\pm 0.93) \times 10^{-11} s/\mathrm{cm}^3$. A BEC was made with a new BEC set up which was built with a steel chamber and a cloverleaf type magnetic trap. Ultracold atoms in a BEC were loaded into a 3-D optical lattice and a quantum phase transition from a superfluid to a Mott insulator was studied. A TOF absorption imaging was used to study this transition. In a superfluid state, matter wave interference pattern was observed and in a Mott insulator state, there was no matter wave interference pattern. Careful study of the central peak width change showed the increase of width when the system enters a Mott insulator state.

A Raman photoassociation was used to produce ultracold molecules from a Mott insulator. A Raman resonance frequency shift between two atoms per site Mott insulator and three atoms per site Mott insulator was observed. By locking the Raman resonance frequency onto the two atoms per site Mott insulator resonance, Rabi oscillations between atoms and molecule were observed. Coherent Rabi oscillations show the possibility of creating a molecular quantum gas in an optical lattice.

There are several open questions and possible future experiments based on the current results. To understand a quantum phase transition with trapped atoms, we need to study the effect of inhomogeneity on the transition and especially, the possible formation of several Mott domains in a single system needs to be understood. The central peak width change may be very helpful to study the creation of several Mott domains and a Raman photoassociation will also be a useful tool to determine the population distribution among different Mott domains. From the observance of coherent Rabi oscillations, it is clear that we can create ultracold molecules coherently. Interesting questions will be the nature of many body state of molecules we created. Also it will be interesting to see the possibility of making a molecular BEC by ramping down the optical lattice. Finally, by transferring high-lying vibrational level state molecules into a ro-vibrational ground state molecules, it may be possible to create a real ro-vibrational ground state molecular BEC.

Bibliography

[1] D.R. Tilley, and J. Tilley, *Superfluidity and Superconductivity*, Adam Hilger, Bristol and New york (1990).

[2] Harold J. Metcalf, and Peter van der Straten, *Laser Cooling and Trapping*, Springer-Verlag, New York 1999

[3] M. H. Anderson, and J. R. Ensher, and M. R. Matthews, and C. E. Wieman and E. A. Cornell, *Science* **269**, 198 (1995).

[4] K.B. Davis *et al.*, Phys. Rev. Lett. **75**, 3969 (1995).

[5] M. Inguscio, S. Stringari, and C.E. Wieman (eds), *Proceedings of the International School of Physics ¡¡Enrico Fermi¿¿, Course CXL,* IOS Press, Amsterdam, p. 3 (1999).

[6] D. deMarco and D. S. Jin, *Science* **285**, 1703 (1999).

[7] K. M. O'Hara *et al.*, *Science* **298**, 2179 (2002).

[8] C. A. Regal and D. S. Jin, Phys. Rev. Lett. **90**, 230404 (2003).

[9] N. Balakrishnan, and A. Dalgarno, Chem. Phys. Lett. **341**, 652 2001

[10] D. DeMille, Phys. Rev. Lett. **88**, 071805 2002

[11] D. Egorov, J. D. Weinstein, D. Patterson, B. Friedrich, and J. M. Doyle, Phys. Rev. A **63**, 030501 2001

[12] L. Santos, G. V. Shlyapnikov, P. Zoller, and M. Lewenstein, Phys. Rev. Lett. **85**, 1791 2000

[13] D.J. Heinzen, R. Wynar, P.D. Drummond, and K.V. Kherunstyan, Phys. Rev. Lett. **84**, 5029 (2000).

[14] J.D. Weinstein, R. deCarvalho, T. Guillet, B. Friedrich, and J.M. Doyle, *Nature* **395**, 148 (1998).

[15] H.L. Bethlem, G. Berden, F.M.H. Crompvoets, R.T. Jongma, A.J.A. van Roij, and G. Meijer, *Nature* **406**, 491 (2000).

[16] P. Courtielle, R.S. Freeland, D.J. Heinzen, F.A. van Abeelen, and B.J. Verhaar, Phys. Rev. Lett. **81** 69 (1998).

[17] J.L. Roberts, N.R. Caussen, J.P. Burke, C.H. Greene, E.A. Cornell, and C.E. Wieman, Phys. Rev. Lett. **81**, 5109 (1998).

[18] S. Inouye, M.R. Andrews, J. Stenger, H.J. Miesner, D.M. Stamper-Kern, and W. Ketterle, *Nature* **392**, 151 (1998).

[19] J.D. Miller, R.A. Cline, and D.J. Heinzen, Phys. Rev. Lett. **71**, 2204 (1993).

[20] P.D. Lett, K. Helmerson, W.D. Phillips, L.P. Ratliff, S.L. Rolston, and M.E. Wagshul, Phys. Rev. Lett. **71**, 2200 (1993).

[21] T. Takekoshi, B.M. Patterson, and R.J. Knize, Phys. Rev. A **59**, R5 (1999).

[22] A. Fioretti, D. Comparat, A. Crubellier, O. Delieu, F. Masnou-Seeuws, and P. Pillet, Phys. Rev. Lett. **80**, 4402 (1998).

[23] A.N. Nikolov, E.E. Eyler, X.T. Wang, J. Li, H. Wang, W.C. Stwalley, and P.L. Gould, Phys. Rev. Lett. **82**, 703 (1999).

[24] A.N. Nikolov, J.R. Ensher, E.E. Eyler, H. Wang, W.C. Stwalley, and P.L. Gould, Phys. Rev. Lett. **84**, 246 (2000).

[25] C. Gabbanini, A. Fioretti, A. Lucchesini, S. Gozzini, M. Mazzoni, Phys. Rev. Lett. **84**, 2814 (2000).

[26] Nicolas Vanhaecke, Wilson de Souza Melo, Bruno Laburthe Tolra, Daniel Comparat, and Pierre Pillet Phys. Rev. Lett. **89**, 063001 (2002).

[27] E.A. Donley *et al.*, *Nature* **417**, 529 (2002).

[28] D. Jaksch, C. Bruder, J.I. Cirac, C.W. Gardiner, and P. Zoller, Phys. Rev. Lett. **81**, 3108 1998

[29] M. Greiner, O. Mandel, T. Esslinger, T. Hansch, and I. Bloch, *Nature* **415**, 30, 2002

[30] E. Demler, and F. Zhou, Phys. Rev. Lett. **88**, 163001 (2002).

[31] A. B. Kukolv, and B. V. Svistunov, Phys. Rev. Lett. **90**, 100401 (2003).

[32] D. Jaksch, H. -J. Briegel, J. I. Cirac, C. W. Gardiner, and P. Zoller, Phys. Rev. Lett. **82**, 2022 (1999).

[33] , M.D. Girardeau, Phys. Rev. B **139**, 500 (1965).

[34] , K. V. Kheruntsyan, D. M. Gangardt, P. D. Drummond, and G. V. Shlyapnikov, Phys. Rev. Lett. **91**, 040403 (2003).

[35] , W. Hofstetter, *et al.*, Phys. Rev. Lett. **89**, 229407 (2002).

[36] , Carsten Hornerkamp and Walter Hofstetter, Phys. Rev. Lett. **92**, 170403 (2004).

[37] D.J. Han, Ph.D. Thesis, The University of Texas (1998).

[38] R.H. Wynar, Ph.D. Thesis, The University of Texas (2000).

[39] W. Ketterle, D.B. Davis, M.A. Joffe, A. Martin, and D.E. Prichard, Phys. Rev. Lett. **70**, 253 (1993).

[40] Riley Freeland, Ph.D. Thesis, The University of Texas (2001).

[41] R. Wynar, R.S. Freeland, D.J. Han, C. Ryu, and D.J. Heinzen, *Science* **287**, 1016 (2000).

[42] P. Soldan, M.T. Cvita, J.M. Hustion, P. Honvault, and J.-M. Launay, Phys. Rev. Lett. **89**, 153201 (2002).

[43] T. Mukaiyama, J. Abo-Shaeer, K. Xu, J. Chin, and W. Ketterle, Phys. Rev. Lett. **92**, 180402 (2004).

[44] Subir Sachedev, *Quantum Phase Transitions*, Cambridge University Press (1999).

[45] M.P.A. Fisher, P.B. Weichman, G. Grinstein, and D.S. Fisher, Phys. Rev. B **40**, 546 1989

[46] G.G. Batrouni, R.T. Scalettar, and G.T. Zimanyi, Phys. Rev. Lett. **65**, 1765 1990

[47] P. Niyaz, R.T. Scalettar, C.Y. Fong, and G.G. Batrouni, Phys. Rev. B **50**, 362 1994

[48] A. van Oudenaarden, and J.E. Mooij, Phys. Rev. Lett. **76**, 4947 1996

[49] G.T. Zimanyi, P.A. Crowell, R.T. Scalettar, and G.G. Batrouni, Phys. Rev. B **50**, 6515 1994

[50] L. Deng, E. W. Hagley, J. Denschlag, J. E. Simsarian, M. Edwards, C. W. Clark, K. Helmerson, S. L. Rolston, and W. D. Phillips, Phys. Rev. Lett. **83**, 5407 1999

[51] Yu. B. Ovchinnikov, J. H. Muller, M. R. Doery, E. J. D. Vredenbregt, K. Helmerson, S. L. Rolston, and W. D. Phillips, Phys. Rev. Lett. **83**, 284 1999

[52] Thilo Stoferle, Henning Moritz, Christian Schori, Michael Kohl, and Tilman Esslinger, Phys. Rev. Lett. **92**, 130403 2004

[53] C. Kollath, U. Schollwock, J. von Delft, and W. Zwerger, Phys. Rev. A **69**, 031601(R) 2004

[54] C. A. Regal, M. Greiner, and D. S. Jin, Phys. Rev. Lett. **92**, 083201 2004

[55] M. Greiner, C. A. Regal, and D. S. Jin, *Nature* **426**, 537 2003

[56] C. A. Regal, C, Ticknor, J. L. Bohn, and D. S. Jin, *Nature* **424**, 47 2003

[57] D. Jaksch, V. Venturi, J. I. Cirac, C. J. Williams, and P. Zoller, Phys. Rev. Lett. **89**, 040402 2002

[58] M. Kramer, L. Pitaevski, and S. Stringari, Phys. Rev. Lett. **88**, 180404 2002

[59] P. Rabl, A. J. Daley, P. O. Fedichev, J. I. Cirac, and P. Zoller Phys. Rev. Lett. **91**, 110403 2003

Vita

Changhyun Ryu was born in Che-ju, Korea on April 20, 1970. He attended Seoul National University and received B.S. and M.S. degree in physics. In August 1998, he entered the graduate school of the University of Texas.

Permanent address: 1646 W. 6th St. APT L
Austin, Texas 78703

This dissertation was typeset with LaTeX[†] by the author.

[†] LaTeX is a document preparation system developed by Leslie Lamport as a special version of Donald Knuth's TeX Program.